

## Review

# Surface Modification of 42CrMo Steels: A Review from Wear and Corrosion Resistance

Zhendong Zhang <sup>1,2,3</sup>, Di Wang <sup>1</sup>, Guanglei Liu <sup>4</sup>, Yiyi Qian <sup>1</sup>, Yuquan Xu <sup>1</sup> and Dingding Xiang <sup>1,2,3,\*</sup>

<sup>1</sup> School of Mechanical Engineering and Automation, Northeastern University, Shenyang 110819, China; 2270285@stu.neu.edu.cn (Z.Z.); wxd\_990511@163.com (D.W.)

<sup>2</sup> State Key Laboratory of Solid Lubrication, Lanzhou Institute of Chemical Physics, Chinese Academy of Sciences, Lanzhou 730000, China

<sup>3</sup> Foshan Graduate School of Innovation, Northeastern University, Foshan 528311, China

<sup>4</sup> Research and Development Department, Jianlong Beiman Special Steel Co., Ltd., Qiqihar 161041, China; lgl8218@163.com

\* Correspondence: xiangdd@mail.neu.edu.cn

**Abstract:** This work reviews surface modification techniques for improving the wear and corrosion resistance of 42CrMo steel. The advantages and disadvantages of various methods, including thermal spraying, deposition, hardfacing, laser cladding, nitriding, and laser surface treatment, are discussed. The review elaborates on the materials commonly employed in laser cladding technology, including iron-based, cobalt-based, nickel-based, and high-entropy alloys and reinforced composite coatings. Furthermore, the mechanisms and methods of improving the wear and corrosion resistance of 42CrMo steel are summarized. Finally, this review presents research shortcomings and future opportunities of surface modification techniques. This review also provides a theoretical guide for the application of 42CrMo steel.

**Keywords:** 42CrMo; surface modification; wear resistance; corrosion resistance; self-lubricating



**Citation:** Zhang, Z.; Wang, D.; Liu, G.; Qian, Y.; Xu, Y.; Xiang, D. Surface Modification of 42CrMo Steels: A Review from Wear and Corrosion Resistance. *Coatings* **2024**, *14*, 337. <https://doi.org/10.3390/coatings14030337>

Academic Editor: Antonio Ancona

Received: 20 January 2024

Revised: 5 March 2024

Accepted: 7 March 2024

Published: 12 March 2024



**Copyright:** © 2024 by the authors. Licensee MDPI, Basel, Switzerland. This article is an open access article distributed under the terms and conditions of the Creative Commons Attribution (CC BY) license (<https://creativecommons.org/licenses/by/4.0/>).

## 1. Introduction

A 42CrMo steel is a medium carbon steel containing Cr and Mo, giving it excellent hardenability and toughness. The chemical composition of 42CrMo is shown in Table 1. This 42CrMo steel is commonly used for various general-purpose parts, such as crankshafts, rams, spindles, gears, press brake dies, casting rolls, hydraulic pistons, chain sprocket wheels, cutting tools, bearings, etc. [1–4]. The surface of this steel is prone to wear and corrosion, which results in shortening its service life. Therefore, improving the surface properties of 42CrMo steel has been a topic of extensive research.

Surface modification technology is necessary to enhance the service life of industrial machinery components by improving their surface properties, thereby reducing the damage and potential failure caused by wear and corrosion. Figure 1a shows the number of surface modification techniques applied to 42CrMo steel. Laser cladding has received a lot of attention compared to other techniques because of its high energy density, controllable dilution rate, fast processing speed, small heat-affected zone, small deformation, and high solidification rate. Similarly, the material used to cover the 42CrMo steel in Figure 1b is primarily formed using laser cladding techniques. Iron-based materials have gained significant attention due to their similar composition to 42CrMo steel, robust bonding capabilities with 42CrMo steel, and lower cost compared to nickel-based and cobalt-based materials.

This paper focuses on the current status of research on surface modification of 42CrMo steel. The first part introduces 42CrMo steel and its related rate of coverage in the literature. The second part describes the current surface modification techniques applied to 42CrMo steel. The third part describes the material systems applied to the surface of 42CrMo steel. The fourth and fifth parts describe the mechanism of improving the wear resistance and

corrosion resistance of 42CrMo steel, respectively. The last part is the conclusion and outlook. In particular, the second part of this paper describes thermal spraying, deposition, hardfacing, laser cladding, nitriding, and laser surface treatment in turn. Subsequently, this text introduces iron-based, cobalt-based, nickel-based, and high-entropy alloys and reinforced composite coatings, with a focus on laser cladding technology. According to the coating properties, the mechanisms to improve the wear resistance of the coatings are reviewed to improve the macro- and microstructure of the coatings and to form a self-lubricating coating on the surface of the coatings. Coating corrosion resistance mechanisms are also reviewed, which include the formation of corrosion-resistant coatings on the surface, the improvement of macroscopic defects and microstructures, and the formation of passivation films. In the concluding part of this paper, the important findings for 42CrMo steels are summarized and future research directions are discussed.

**Table 1.** The chemical composition of 42CrMo steel (mass fraction, wt.%).

| C         | Si        | Mn        | Cr        | Mo        | S      | P      | Fe   |
|-----------|-----------|-----------|-----------|-----------|--------|--------|------|
| 0.38–0.45 | 0.17–0.37 | 0.50–0.80 | 0.90–1.20 | 0.15–0.25 | ≤0.035 | ≤0.035 | Bal. |

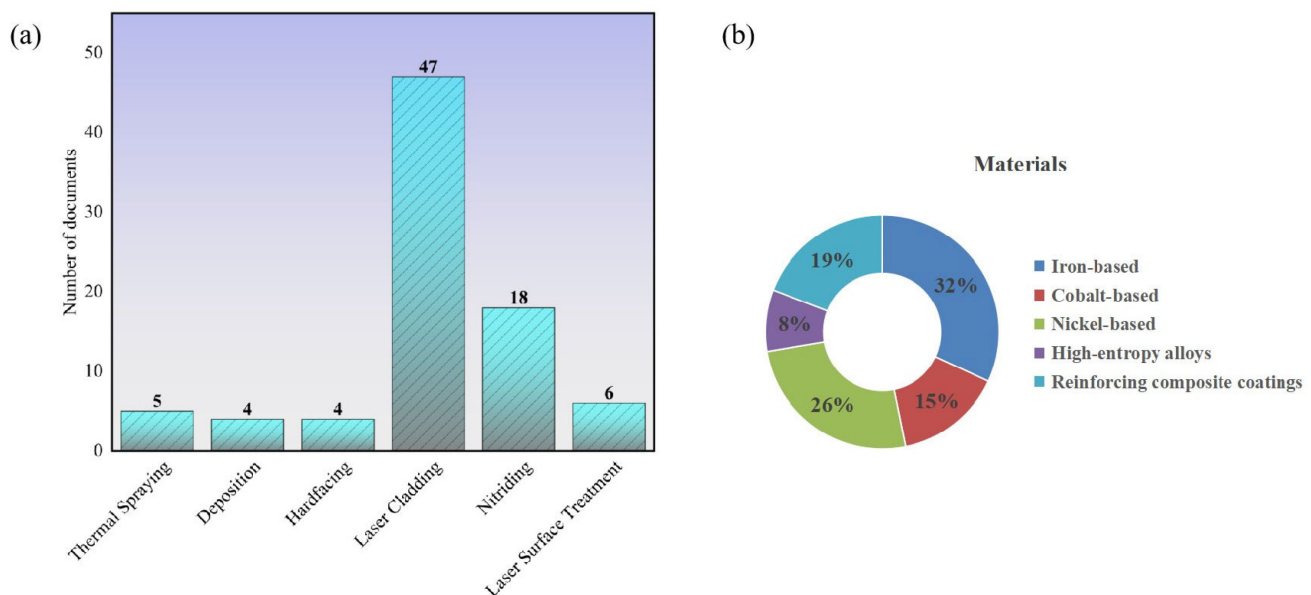


**Figure 1.** (a) Number of publications for each surface modification technique applied to 42CrMo steel; (b) percentage of the number of surface coating materials applied to 42CrMo steel.

It should be emphasized that this review is different from other review articles in that this review takes a single material, 42CrMo steel, as the object of study. However, this thesis provides some inspiration for other steel materials, and the discoveries in surface modification techniques and materials mentioned in this thesis can be applied to other steel surfaces to improve wear and corrosion resistance.

## 2. Surface Modification

The advantages and disadvantages of the surface modification techniques applied to 42CrMo steel are shown in Table 2, and the mechanism of the techniques is shown in Figure 2. Thermal spraying offers a wide array of applications and enables precise control over coating thickness, but it has some drawbacks, such as poor bonding strength, high porosity, and susceptibility to workpiece deformation. Deposition techniques excel in producing dense, uniform coatings with strong bonding properties but typically yield thinner coatings. Hardfacing enhances surface durability, reducing replacement costs, yet the resultant high coating hardness may lead to brittleness. Nitriding improves wear

and corrosion resistance and primarily suitable for iron-based alloys, but it is a high-temperature process. Laser cladding boasts high energy density, controlled dilution rates, rapid processing, minimal heat-affected zones, and low distortion. Laser surface treatment allows for localized treatment, minimizing heat-affected zones. Nonetheless, the initial investment in equipment for both technologies remains substantial.

**Table 2.** Comparison of the advantages and disadvantages of modification technology [5].

| Technology              | Advantages  | Disadvantages  |
|-------------------------|---|--|
| Thermal spraying        | Wide range of applications, controlled coating thickness  | Poor bonding strength, porosity, and workpiece deformation                 |
| Deposition              | Suitable for depositing on dense, uniform materials; strong bonding force   | Expensive equipment, thin coating thickness                                |
| Hardfacing              | Tough and wear-resistant surface, reducing replacement costs  | High hardness leads to brittleness   |
| Laser cladding          | High energy density, controllable dilution rate, fast processing speed, small heat-affected zone, small deformation, high solidification rate | High initial investment for laser systems                                  |
| Nitriding               | Higher wear and corrosion resistance  | Primarily applicable to iron-based alloys, high temperature of the process |
| Laser surface treatment | Allows for localized treatment, minimizes heat-affected zones   | Initial investment in laser equipment can be high                          |

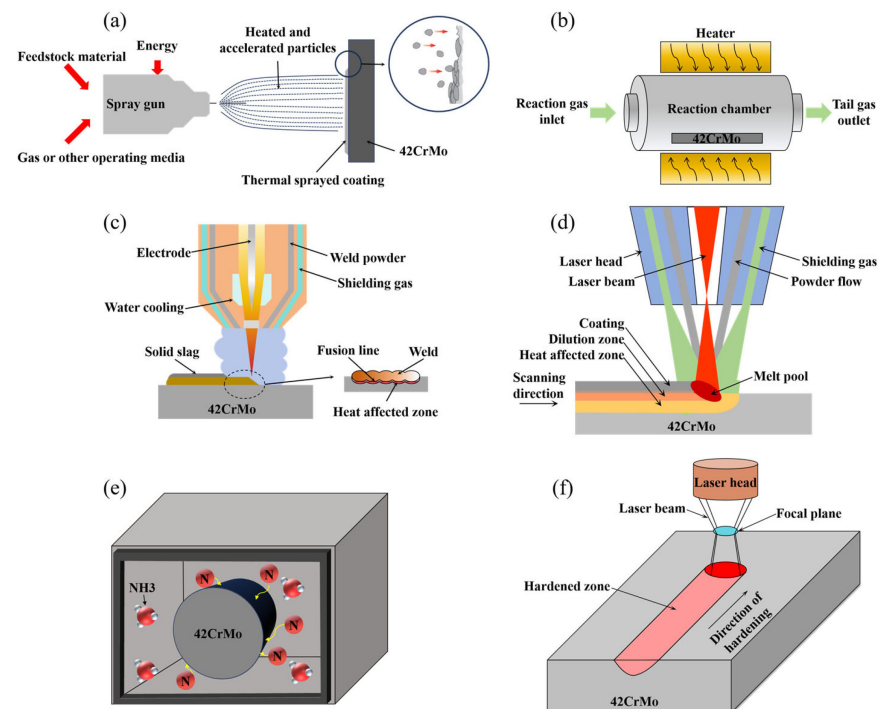


**Figure 2.** Mechanism of each surface modification technology: (a) thermal spraying; (b) chemical vapor deposition; (c) hardfacing; (d) laser cladding; (e) nitriding; (f) laser surface transformation hardening or laser surface melting.

### 2.1. Thermal Spraying

Thermal spraying technology is a highly effective surface modification technique in the field of surface engineering [6]. The main thermal spraying techniques applied to 42CrMo steels include plasma spraying and high-velocity oxygen fuel spraying. Both thermal spraying processes are based on the same principle: rapidly heating the coating material within a hot gas medium and projecting it onto the surface at high velocity to create a coating.

Xu et al. [7] utilized the surface engineering process of plasma spraying to fabricate a composite coating consisting of Co alloy, WC, and Fe-based amorphous alloy on the surface of 42CrMo steel. Their findings demonstrated a complete metallurgical bond between the coatings and the substrate interface. Moreover, the hardness of the coatings exhibited a proportional increase with the mass fraction of the Fe-based amorphous alloy. These results underscored the efficacy of amorphous alloy powders as a beneficial additive in plasma spray welding for coating preparation. Further research in this direction can be carried out to explore other properties of composite coatings.

High-velocity oxygen fuel spraying technology has replaced traditional plasma spraying in many fields due to its advantages, including lower operating temperatures, reduced economic costs, and higher spraying efficiency [8]. Sun et al. [9] prepared WC-17Co coatings on the surface of 42CrMo steel using the surface engineering process of high-velocity oxygen fuel spraying. The impact of heat treatment on the coatings was explored across a temperature range spanning from 500 to 1100 °C. The results demonstrated a reduction in  $W_2C$  phase intensity as amorphous Co underwent recrystallization, accompanied by the formation of new phases such as  $Co_3W_3C$  and  $Co_6W_6C$  upon heat treatment. The porosity distribution exhibited a non-linear trend, initially increasing before declining with higher temperatures. Various discontinuous plate-like oxide films emerged on the coatings' surface after heat treatment, underscoring the significant influence of binder structure on corrosion resistance. Liu et al. [10,11] successfully prepared WC-12%Cr<sub>3</sub>C<sub>2</sub>-6%Ni coatings and WC-12%Co-6%Cr coatings on 42CrMo steel substrates with the surface engineering process of high-velocity oxygen fuel spraying and sealed them with sol-gel aluminum phosphate inorganic sealant. The findings revealed that the application of a sealing treatment could enhance the wear and corrosion resistance of the coatings.

However, thermal spray coatings have unavoidable defects, such as high residual porosity, microcracks, and low adhesion strength, which limit their application range. Reducing manufacturing defects through defect detection can improve surface quality and mechanical properties [12]. To address these defects, remelting treatment can be employed to enhance the adhesion strength and eliminate the splashing boundaries of the coating, consequently improving its resistance to wear and corrosion [13,14]. Chen et al. [15] enhanced the in situ TiN-reinforced NiCrBSi composite coating, achieved by spraying NiCrBSi alloy and Ti powders, through induction remelting. This process rectified defects, enhanced interlamellar bonding, transformed bonding mechanisms to metallurgical bonds, and bolstered the coatings' resistance to sliding wear and particle erosion.

## 2.2. Deposition

The main deposition methods applied to 42CrMo steels are electrodeposition and chemical vapor deposition. Electrodeposition is a dependable method for acquiring nanostructured coatings with superior mechanical and electrochemical properties [16]. The most recent advancement regarding deposition techniques applied to 42CrMo steels is the electrodeposition technique. Zhang et al. [17] deposited various CoNiP alloy coatings on the surface of 42CrMo steel using different concentrations of sodium hypophosphite solution. The findings indicated that the CoNiP alloy coatings exhibited a granular structure. The introduction of sodium hypophosphite into the solution not only hastened the chemical reaction rate but also enhanced the thickness of the coating and refined the surface particles, thereby improving the wear resistance.

Chemical vapor deposition is a method wherein volatile compound gases of the coating material decompose or chemically react, depositing a film onto the workpiece. This process minimizes the impact on the substrate's hardness, yielding a dense coating with low internal stress, robust adhesion, exceptional uniformity, and complete coverage of complex-shaped parts. However, the applicability of this technology is constrained by substrates unable to endure high temperatures, as well as parts prone to deformation. Additionally, diffusion layers may form, necessitating treatment of exhaust gases. Nevertheless, this technology can be utilized to modify the micromotional wear behavior of metallic materials

by enhancing the hardness of contact surfaces and diminishing the friction coefficient within the micromotional zone. Zhang et al. [18] utilized the surface engineering process of chemical vapor deposition to prepare TiC/Ti (CN)/TiN multilayer coatings on the surface of 42CrMo steels. This method presents enhanced opportunities to modify surface properties compared to single-layer films. Examination of the coatings' cross-sectional morphology revealed an approximate thickness of 11  $\mu\text{m}$ , characterized by dense, non-porous structures firmly adhered to the substrate. Moreover, the coatings exhibited an average nano-hardness five times higher than that of the substrate. These Ti-based hard coatings (TiN, TiC, Ti (CN)) demonstrated high hardness levels, superior abrasion resistance, and exceptional chemical stability.

### 2.3. Hardfacing

Hardfacing is a surface treatment technique aimed at enhancing the properties of metals. It serves as an efficient means to lower replacement costs and minimize downtime. The process requires depositing a welded metal on the surface of a substrate and is known for its superior wear and oxidation resistance. Surface hardfacing technology is predominantly employed on components subjected to wear and abrasive environments, safeguarding them and prolonging their lifespan [19]. Y. X. Yu et al. [20] used the surface engineering process of hardfacing instead of the traditional manufacturing process to deposit D322 on 42CrMo steel. The experimental findings suggest that the hardfacing surface exhibited excellent configuration with no obvious defects. Its properties either met or surpassed those of dies manufactured using traditional methods. With an average hardfacing layer exceeding 57.5 HRC, it delivered commendable wear resistance at a reduced cost. M.A. Morsy et al. [21] introduced an austenite cushion layer between the base metal and the hardfacing alloy. This approach effectively eliminated cracks in the base metal and interfacial regions, substantially reducing the occurrence of weld metal cracks.

Chen et al. [22] integrated nano  $\text{TiO}_2$  particles into the materials of hardfacing, revealing that the grain size gradually diminished with higher concentrations of nano  $\text{TiO}_2$ . This led to a more homogeneous dispersion of carbides and a modification of the carbide morphology. At a nano  $\text{TiO}_2$  content of 0.8 wt.%, the particles displayed a network distribution along the grain boundaries. Furthermore, the hardness of the hardfacing alloys peaked at 56.4 HRC with a nano  $\text{TiO}_2$  content of 0.6 wt.%. However, in that study, nano  $\text{TiO}_2$  with 0.4 wt.% content was not investigated, so it was not possible to compare its effect with that of 0.6 wt.%.

### 2.4. Laser Cladding

The laser cladding (LC) process is also known as direct metal deposition, laser engineered net shaping, laser additive manufacturing, laser metal deposition, or direct energy deposition [23]. Powder utilizes absorbed laser energy to deposit a fused cladding layer with improved properties on a given substrate. There are various methods of material deposition, among which coaxial powder feeding is generally considered the most effective method of material deposition, as shown in Figure 2d. LC involves scanning the substrate surface with a high-power laser beam to generate a molten pool while simultaneously injecting powder material into the pool, forming a fusion track upon solidification. LC offers numerous advantages, including metallurgical bonding between the coating and substrate, refinement of the microstructure, a controllable dilution rate, minimal heat-affected zones, and selective cladding of small areas. It is widely employed in surface treatment and localized remanufacturing repair of critical components in industries such as aerospace, metallurgy, coal power, automobile manufacturing, and various other fields.

Table 3 shows the LC process parameters and coating properties used in each study. The process parameters directly influence the laser's interaction with the powder and substrate, affecting mobility, convection, mass melt transfer, and grain alterations. Laser power is closely associated with the heat input during the cladding process. Excessive laser power can lead to heightened surface roughness of the cladding coating, attributed



to disturbances in the molten pool and gas absorption. Additionally, heat transfer to the substrate can result in an increase in the dilution rate, impacting the surface morphology and chemical composition of the cladding coating [24,25]. When the laser power is too low, the cladding material may not fully melt, resulting in poor wettability between the molten cladding materials and the substrate, leading to inadequate formation of the cladding coating. Additionally, insufficient laser energy is absorbed by the substrate surface, hindering the formation of a robust metallurgical bond between the substrate and the cladding coating [26]. The scanning speed plays a significant role in determining the height of the cladding layer [27]. Appropriate process parameters can help minimize the occurrence of internal defects and enhance the quality of the molding. Cheng et al. [3] demonstrated that reducing the scanning speed while keeping the energy density constant (laser power/scanning speed) led to a higher-quality cladding layer. This improvement in quality was attributed to factors such as the presence of martensite, fine crystals, solid solution, and precipitated phases, which contribute to an increase in the microhardness of the coating. The cladding layer typically had a thickness of approximately 1.8 mm, with the microhardness ranging between 210 and 450 HV, which was two to three times greater than that of the substrate.

**Table 3.** LC process parameters using 42CrMo steel as a substrate.

| Laser Power (W)    | Scanning Speed (mm/s) | Powder Feed Rate (g/min) | Spot Diameter (mm) | Shielding Gas (L/min) | Track Overlap (%)      | Ref. |
|--------------------|-----------------------|--------------------------|--------------------|-----------------------|------------------------|------|
| 3000, 5000, 8000   | 2, 5, 8, 10           | 10                       | 3 × 24             | N/A                   | 50                     | [3]  |
| 1000–3000          | 2–6                   | 10–20                    | 5 × 5              | 15                    | N/A                    | [27] |
| 1100               | 3                     | N/A                      | 3                  | N/A                   | N/A                    | [28] |
| 1300               | 3                     | N/A                      | 3                  | 0.22                  | N/A                    | [29] |
| 1300               | 3                     | N/A                      | 3                  | 0.2                   | N/A                    | [30] |
| 1100               | 4                     | N/A                      | 4                  | N/A                   | 50                     | [31] |
| 1500–1900          | 2–4                   | N/A                      | 3–5                | N/A                   | N/A                    | [32] |
| 2200–2400          | 5                     | 14                       | 5                  | N/A                   | 50                     | [33] |
| 3600               | 5                     | 16                       | 7                  | N/A                   | 50                     | [33] |
| 2200–2400          | 5                     | 15                       | 5                  | N/A                   | N/A                    | [34] |
| 1800               | 4                     | N/A                      | 7.4                | 15                    | N/A                    | [35] |
| 1400–1800          | 6–7.3                 | 1.2 r/min                | 3                  | N/A                   | N/A                    | [36] |
| 4000               | 13.3                  | 48.5                     | 6                  | 10                    | N/A                    | [37] |
| 2000–2200          | 5                     | N/A                      | N/A                | N/A                   | N/A                    | [38] |
| 1800               | 14                    | N/A                      | 4                  | 12                    | 40                     | [39] |
| 600                | 6–10                  | 3.6–5.4                  | 1.6                | N/A                   | N/A                    | [40] |
| 800–1200           | 5                     | 2.1                      | N/A                | N/A                   | N/A                    | [41] |
| 1800/1200 (remelt) | 6.7/13.3 (remelt)     | 40                       | 3                  | 10                    | 50                     | [42] |
| 2100               | 200–400               | 7.9                      | 3                  | N/A                   | 50                     | [43] |
| 1300               | 3                     | N/A                      | 3                  | 0.2                   | N/A                    | [44] |
| 800                | 3                     | N/A                      | 3                  | 10                    | N/A                    | [45] |
| 1200               | 6.7                   | 8 L/min                  | 1                  | 10                    | N/A                    | [46] |
| 1000               | 6                     | N/A                      | 4.5                | 20                    | N/A                    | [47] |
| 1800–2800          | 2–4                   | 5–15                     | 3–5                | N/A                   | N/A                    | [48] |
| 1600               | 4                     | 18                       | 3                  | 16                    | 40                     | [49] |
| 1800               | 4                     | N/A                      | 7.2                | 10                    | N/A                    | [50] |
| 1800               | 36                    | N/A                      | N/A                | 6                     | Axial offset 0.32 mm/r | [51] |
| 2000               | 4                     | 15                       | 5 × 5              | 15                    | N/A                    | [52] |
| 2000               | 7                     | 14.41                    | 16                 | 20                    | 30                     | [53] |
| 1500–3500          | 4                     | 15                       | N/A                | N/A                   | 40                     | [54] |

Table 3. Cont.

| Laser Power (W) | Scanning Speed (mm/s) | Powder Feed Rate (g/min) | Spot Diameter (mm) | Shielding Gas (L/min) | Track Overlap (%) | Ref. |
|-----------------|-----------------------|--------------------------|--------------------|-----------------------|-------------------|------|
| 1500–1900       | 2–4                   | N/A                      | 3–5                | N/A                   | N/A               | [55] |
| 2000            | 4                     | 15                       | N/A                | 15                    | N/A               | [56] |
| 4000            | 25                    | N/A                      | N/A                | 10                    | 30                | [57] |
| 1800            | 2                     | N/A                      | 5                  | 10                    | 45                | [58] |
| 3000–5500       | 30–60                 | N/A                      | 4.6                | 20                    | N/A               | [59] |
| 2880            | 7                     | 14                       | 6                  | 8                     | N/A               | [60] |
| 1500–2500       | 2–6                   | 10–20                    | 5×5                | N/A                   | N/A               | [61] |
| 1000            | 5                     | N/A                      | 2                  | 5                     | N/A               | [62] |
| 2000–2300       | 6–9                   | N/A                      | N/A                | N/A                   | 30–40             | [63] |
| 2000            | 3                     | 17.5                     | 5×2                | 15                    | N/A               | [64] |
| 1800            | 5                     | 8                        | 3                  | N/A                   | N/A               | [65] |
| 1900–3200       | 5, 10, 15             | 11–18                    | N/A                | N/A                   | 45                | [66] |

Studies have demonstrated that incorporating external field assistance (magnetic, electric, and ultrasonic fields) into the LC process can reduce defects in the cladding layer, refine its structure, ensure uniform element distribution, lower the friction coefficient, and enhance microhardness and wear resistance [28]. Furthermore, the magnetostrictive effect induced by the magnetic field can diminish thermal expansion and stress, thereby lowering the crack sensitivity of the fused cladding layer [29,30]. In a study by Jiang et al. [31], a 3540Fe/CeO<sub>2</sub> LC layer was prepared on a 42CrMo substrate with in situ ultrasonic vibration assistance. The study examined the influence of the ultrasonic vibration angle on the microstructure evolution and mechanical properties of the LC coating. The results indicated that ultrasonic vibration refined the organization of the fused cladding layer, distributed the elements uniformly, and improved the microhardness. The utilization of ultrasonic vibration proved beneficial in reducing the friction coefficient and enhancing wear resistance. The most significant reduction in the friction coefficient was observed when ultrasonic vibration was applied at a 45° angle. Hu et al. [32] investigated the synergistic effects of ultrasonic, alternating magnetic, and direct current electric fields to enhance laser surface fusion cladding, and examined their impact on molten pool fluid dynamics. Their findings revealed that electromagnetic force and ultrasonic fields can significantly alter fluid flow patterns within the melt pool, leading to uniform grain refinement and homogeneous elemental distribution in the molten cladding layer. Despite the promising results, these techniques are hindered by their complexity and high cost, rendering them impractical for large-scale part fabrication. The main influencing factors should be found through exploration and selection so that they can be applied in practice.

### 2.5. Nitriding

Nitriding, categorized under chemical heat treatment in the ferrite state, involves low treatment temperatures, typically equivalent to or lower than the tempering temperature range of quenched steel. Nitrogen atoms diffuse into the material within temperatures ranging from 480 to 600 °C, leading to the creation of a nitride-dominated penetration layer. Nitriding treatment results in the formation of precipitated phases within the diffusion layer of nitrogen atoms. This enhances the surface hardness of the metallic material and improves its fatigue strength and wear resistance.

Plasma nitriding offers remarkable environmental advantages compared to other nitriding techniques. The nitriding layer comprises an outermost compound layer and a diffusion zone between the compound layer and the substrate. This layer effectively prevents premature failure, extends the service life, and enhances the surface hardness, wear resistance, and corrosion properties of various steels, including low-alloy steels [67,68]. In the plasma nitriding process, the components to be treated are exposed to a high cathode potential, while the grounded wall of the furnace serves as the anode. These components actively participate in the discharge process. The voltage applied between the anode

and cathode typically falls within the range of 400–700 V. Within the cathode fall region near the cathode surface, positive ions generated by glow discharge undergo acceleration and subsequently bombard the surface of the specimen. This ion bombardment induces sputtering, transfers kinetic energy to the component, and elevates its temperature [69].

The thickness of the nitrided layer generated by plasma nitriding can pose challenges to the wear resistance of heavily loaded components. If the composite layer is too thin, the surface hardness and effective hardened layer may not meet performance requirements. Conversely, if the composite layer becomes too thick, it could become brittle and susceptible to cracking and crushing, leading to premature component failure and reduced expected service life of the workpieces [70]. Therefore, scholars have developed nitriding improvement techniques aimed at circumventing the drawbacks associated with conventional plasma nitriding. When 42CrMo steel is nitrided under anode and cathode potentials, the thickness and phase composition of the compound layer are nearly identical. Moreover, there is no significant disparity observed in its microhardness profile and anodic polarization behavior [69]. Plasma nitriding utilizing a hollow cathode source yields a smooth surface with favorable friction properties. Mao et al. [71] and Wu et al. [2] have demonstrated that titanium has a beneficial impact on the nitriding layer. Their research indicates that the newly developed titanium-enhanced plasma nitriding process produces a thinner brittle composite layer, a thicker effective hardened layer, and a nitriding layer with higher hardness compared to conventional plasma nitriding on 42CrMo steel.

Moreover, treating 42CrMo steel before or after nitriding can lead to elevated surface properties. Utilizing laser shock peening alone or in combination with pre-oxidation as a pretreatment enhances the thickness and hardness of the nitriding layer, with the latter approach proving to be more effective [72,73]. Hybrid surface treatments, integrating plasma nitriding with pre-shot peening operations, have been suggested to enhance nitriding efficiency [74]. The diffusion zones in specimens treated with shot peening combined with plasma nitriding were discovered to be nearly twice as thick as those in specimens treated solely by plasma nitriding. This led to improvements in both hardness and wear resistance. Additionally, the application of electrolytic aluminum nitrate to deposit an aluminum hydroxide film on the surface before nitriding resulted in the formation of a compound layer and an effective hardened layer. The thickness of the layer was six times that of conventional plasma nitriding alone, thereby significantly enhancing hardness [75,76]. Pre-oxidation in air prior to plasma nitriding was performed [77,78]. During the pre-oxidation process, uniform nano iron oxide particles were formed on the surface, accompanied by nanocracks and nanopores. This led to a significant increase in surface free energy, optimizing the subsequent plasma nitriding process and facilitating the conversion of oxides to nitrides. As a result, the composite layer thickness increased by more than twice compared to samples without a pre-oxidized composite layer.

M. Mirjani et al. [79] demonstrated that the surface engineering process of plasma nitriding led to the formation of iron nitride phases  $\epsilon$  and  $\gamma'$ , alongside iron oxide phases such as magnetite and hematite. Subsequent post-oxidizing treatment further enhanced the corrosion characteristics of the nitrided compound layer, resulting in the lowest corrosion rate observed [80,81].

## 2.6. Laser Surface Treatment

Laser surface treatment utilizes a laser as an energy source to modify the properties and structure of a material's surface. This method is distinguished by its high energy density, precise control, flexibility, and precision. Specifically, laser surface treatment technologies applied to 42CrMo steels mainly include laser surface hardening and laser surface melting.

The laser beam employed in laser surface hardening swiftly heats the material's surface. This method has garnered attention in the automotive and machine tool sectors owing to its numerous advantages, such as rapid hardening, minimal deformation post-hardening, automation feasibility, and selective hardening capabilities for specific parts. Wang et al. [1]



produced hardened zones via the surface engineering process of laser surface hardening. The resulting hardness of the hardened zone was 1.6 times higher than that of 42CrMo steel, with the hardened zones reaching a thickness of 1.05 mm. Notably, the martensite within the hardened zone appeared smaller compared to the matrix. It contained numerous low-angle grain boundaries, and the average misorientation of the grains within the hardened zone was significantly higher. This further enhanced the hardness of the hardened zone, particularly near the matrix. The shape of the laser beam during this process was also expected to have a discernible impact on the hardening outcome. Sun et al. [82] conducted an experiment using two different shapes of laser beams. One featured a stripy spot with a uniform-intensity array of spots, while the other had a stripy spot with intensity enhancement at the edges of the entire array of spots. The findings revealed that the latter beam shape resulted in a broader and more uniformly hardened layer, especially noticeable at higher scanning speeds and laser power settings. He et al. [4] investigated the effects of laser power and scanning speed on the depth of the hardened layer of 42CrMo steel in the surface engineering process of laser surface hardening. The study revealed that the depth of the hardened layer increased with higher laser power and lower scanning speed.

Laser surface melting offers several advantages, including minimal distortion, high hardness levels, and a narrow heat-affected zone. This process involves the use of high laser power density to heat and melt specific areas of the metal surface. The molten surface layer undergoes rapid solidification due to the heat absorption reaction and heat conduction from the substrate. Li et al. [83] developed a 3D finite element computational method, based on mathematical models, to analyze the broadband laser surface melting process of 42CrMo. The study investigated the microstructure evolution, hardness distribution, and stress field variations within the melted zone under different laser power settings. Results indicated that increasing the laser power from 3000 to 3800 W led to an expansion in both the width and the depth of the melting layer. However, the variation in laser power showed a negligible impact on the martensite content, which remained consistently above 90% in the hardened zone. Mechanical properties of the melt-hardened zone were significantly influenced by the volume expansion effect, resulting in a notable increase in hardness of two to three times. Additionally, residual stress within the melt-hardened zone consistently manifested as compressive. Furthermore, they [84] devised a numerical model to investigate the influence of the overlap rate on the hardness and stress distribution during multi-pass laser surface melting. The study revealed that the hardness of the initial track within the melting zone experienced a slight decrease due to tempering effects from subsequent tracks. Residual compressive stresses were found to persist within the melting zone following multi-pass laser surface melting. However, tensile stresses at the boundaries of the heat-affected zone and overlap zone could potentially initiate cracks. The maximum stress on the specimen surface decreased as the overlap ratio increased.

### 3. Materials

Selecting the right coating material is the key to obtaining the desired properties and surface quality. It is important to take into account the physicochemical properties of both the substrate and the coating materials. A thorough comprehension of the microstructure–composition–synthesis–processing relationship can be attained through numerous experiments and analyses. This understanding can aid in the optimization of parameters and material systems [85]. The primary emphasis here is on iron-based, cobalt-based, nickel-based, and high-entropy alloys and reinforced composite coatings utilized in LC technologies.

#### 3.1. Iron-Based

Iron-based alloy materials find diverse applications in repairing steel components and are readily accessible from numerous sources [86,87]. The chemical composition of the iron-based powders of each study is shown in Table 4. It mainly consists of Fe, Cr, Mo, W, V, and small amounts of C. The interface created by the coating envelops and forms a

robust bond with the substrate, facilitated by the similarity in composition [88]. The coating primarily comprises sub-stable structures that result in martensitic formation and carbide enhancement, thereby improving hardness and wear resistance [89]. Moreover, iron-based alloys are notably more cost-effective, with prices ranging from 1/4 to 1/5 of nickel-based alloys and 1/8 to 1/9 of cobalt-based alloys, making them more conducive to mass production [90]. However, these alloys are associated with certain drawbacks, including a high melting point, limited fluidity of the molten pool, susceptibility to oxidation, and a propensity to develop cracks, pores, slag, and other defects.

**Table 4.** The iron-based powders of each study (mass fraction, wt.%).

| Materials                                      | C          | Si       | Co      | Cr        | Ni      | B       | Mo        | W         | V         | Nb      | Mn        | P            | S    | Fe   | Ref.     |
|--|------------|----------|---------|-----------|---------|---------|-----------|-----------|-----------|---------|-----------|--------------|------|------|----------|
| Fe-based                                       | 0.10–0.015 | 1.0–1.5  | N/A     | 15–17     | 3.5–4.0 | 0.5–1.1 | 1.5–1.9   | N/A       | N/A       | 1.1–1.7 | 0.3–0.7   | N/A          | N/A  | Bal. | [3]      |
| Fe-based                                       | 0.2        | 0.75     | 0.5     | 16.0      | 2.5     | 1.0     | 0.5       | N/A       | N/A       | N/A     | N/A       | N/A          | N/A  | Bal. | [27]     |
| 3540Fe   | 0.4–0.7    | 4.5      | N/A     | 18–20     | 24–30   | 1.5–2.5 | 4–5       | N/A       | N/A       | N/A     | N/A       | N/A          | N/A  | Bal. | [31]     |
| Fe-Cr-Mo-W-V                                   | 1.40       | 0.40     | N/A     | 4.30      | N/A     | N/A     | 4.0–6.0   | 5.0–6.0   | 3.0–5.0   | N/A     | N/A       | N/A          | N/A  | Bal. | [33]     |
| Fe <sub>bal-x</sub> -Cr-Mo-W-V-Co <sub>x</sub> | 1.40       | 0.40     | 3.0–5.0 | 4.30      | N/A     | N/A     | 4.0–6.0   | 5.0–6.0   | 3.0–5.0   | N/A     | N/A       | N/A          | N/A  | Bal. |          |
| High-carbon                                    | ≥2.0       | ≤0.50    | N/A     | 4.0–6.0   | N/A     | N/A     | 5.0–7.0   | N/A       | 4.0–6.0   | N/A     | N/A       | N/A          | N/A  | Bal. | [34]     |
| HSS  | ≥2.0       | ≤0.50    | N/A     | 4.0–6.0   | N/A     | N/A     | 5.0–7.0   | 5.0–7.0   | 4.0–6.0   | N/A     | N/A       | N/A          | N/A  | Bal. |          |
| Fe-based                                       | 0.7–1      | 1–1.5    | N/A     | 3–4       | N/A     | 0.5–1   | N/A       | 4–6       | 1–2       | 0.5–1   | 1–1.5     | N/A          | N/A  | Bal. | [35]     |
|  | 1.3        | N/A      | N/A     | 4.3       | N/A     | N/A     | 4.6       | 5.6       | 4.0–5.0   | N/A     | N/A       | N/A          | N/A  | Bal. |          |
| HSS  | 1.3        | N/A      | 3.0–5.0 | 4.3       | N/A     | N/A     | 4.6       | 5.6       | 3.0–5.0   | N/A     | N/A       | N/A          | N/A  | Bal. | [38]     |
|  | 1.3        | N/A      | N/A     | 4.2       | N/A     | N/A     | 5.0–6.0   | 6.0–7.0   | 3.0–4.0   | N/A     | N/A       | N/A          | N/A  | Bal. |          |
| Fe55   | 0.7–1.0    | 3.0–0.4  | N/A     | 16–18     | 10–13   | 3.5–4.0 | N/A       | N/A       | N/A       | N/A     | N/A       | N/A          | N/A  | Bal. | [39]     |
| T15  | 1.60       | N/A      | 5.00    | 4.0       | N/A     | N/A     | N/A       | 12.0      | 4.9       | N/A     | 0.3       | N/A          | 0.04 | Bal. | [40]     |
| HSS  | 0.5–1      | N/A      | N/A     | 3–4       | N/A     | N/A     | N/A       | 6–8       | 0.5–1     | 0.5–1   | N/A       | N/A          | N/A  | Bal. | [50]     |
| M2 alloy                                       | 0.95–1.05  | 0.2–0.45 | N/A     | 3.75–4.50 | N/A     | N/A     | 4.50–5.50 | 5.50–6.75 | 1.75–2.20 | N/A     | 0.15–0.40 | P + S ≤ 0.06 |      | Bal. | [51]     |
| T15  | 1.60       | 0.48     | 5.4     | 4.5       | N/A     | N/A     | N/A       | 11.7      | 4.7       | N/A     | 0.45      | N/A          | N/A  | Bal. | [53, 63] |
| Fe-based                                       | 0.9–1.0    | N/A      | N/A     | 1–1.2     | N/A     | 0.1–0.3 | 1.5–2.0   | N/A       | N/A       | N/A     | 8.5–9.0   | N/A          | N/A  | Bal. | [65]     |
| V-rich HSS                                     | 1.8–2.2    | 1.0      | N/A     | 5.2       | N/A     | N/A     | 1.2       | 0.3       | 9.0–12.0  | N/A     | N/A       | N/A          | N/A  | Bal. | [66]     |

Feng et al. [35] demonstrated that the average hardness of M3 (C, B)-enhanced LC iron-based coatings exceeded that of the 42CrMo substrate by 2.5 times, while the abrasion resistance of the coatings was 98.3% higher than that of the 42CrMo substrate. Furthermore, owing to the combined influence of thermal and phase-transition stresses, the residual stress distribution within the coating was predominantly compressive. Notably, residual tensile stress at the interface between the coating and the substrate was minimal, thereby reducing the risk of coating cracking.

N. Ur Rahman et al. [33] conducted LC studies on the microstructure of two high-speed steel (HSS) alloys on 42CrMo steel columnar substrate by optimizing the single-layer LC process. Figure 3d–f display the BSE micrographs and EBSD phase diagrams of LC1 (Fe-Cr-Mo-W-V) coatings, respectively. As depicted in Figure 3, the coating organization consisted of eutectic carbides, a martensitic dendritic intergranular network, and residual austenite. Notably, due to the similarity in the crystal structures, it can be observed in Figure 3a–c that the VC carbide was bonded to the austenite. Upon the transformation of residual austenite to martensite after reheating, a substantial proportion of VC, Mo<sub>2</sub>C, and Cr<sub>23</sub>C<sub>6</sub> carbides was present. The inverse pole figures (Figure 3e,f) reveal a non-uniform distribution of grain orientation. Residual stresses in the LC-deposited HSS were quantified using strain gauges. The findings indicated the existence of compressive residual stresses extending from the top layer to the substrate. This phenomenon was attributed to the significant shrinkage of the fused cladding layer near the interface, resulting from contact with the colder substrate during the reconsolidation process, thus promoting heat conduction. After multiple fusion cladding passes, the microhardness gradually decreased from 795 HV to 570 HV. This decrease in hardness can be attributed to martensitic tempering during the successive fusion cladding process. Introducing a new alloy, Fe<sub>bal-x</sub>-Cr-MoW-V-Co<sub>x</sub>, with 3–5% Co added to Fe-Cr-Mo-W-V, resulted in a co-mingled structure. The hardness of the successive fusion cladding layers increased due to the presence of Co, which formed a solid solution with Fe.

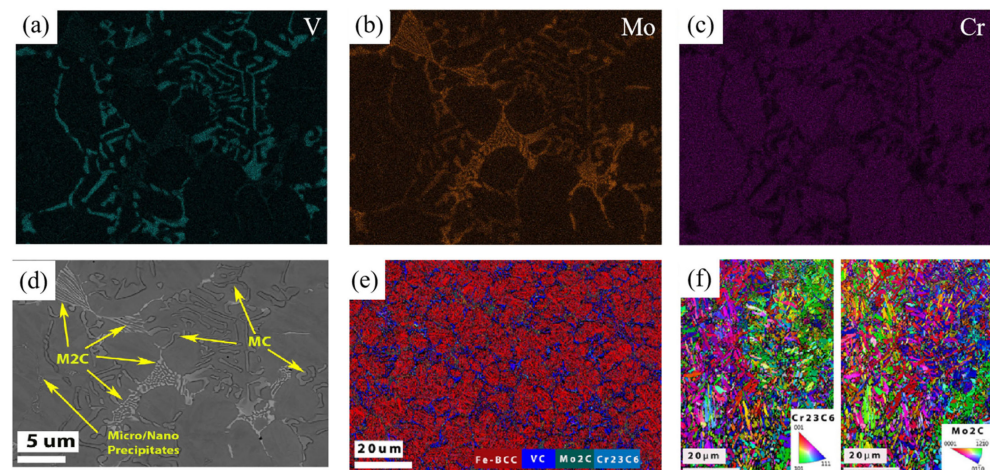


**Figure 3.** (a–c) EDS images; (d) BSE micrograph of the LC HSS alloys; (e,f) EBSD phase map of LC1 and inverse pole figures [33].

During the LC process, the transport phenomena within the molten pool, such as rapid solidification, intense fluid convection, and species diffusion, are intricate and pivotal in shaping the microstructure and composition of the cladding layer. Zhao et al. [40] developed a computational fluid dynamics model of LC on 42CrMo steel with iron-based T15 powder and T15/CeO<sub>2</sub> hybrid powder. They employed a combined horizontal collector volume method to forecast the free surface of the melt pool. Simulation outcomes indicate that the melt pool was chiefly influenced by robust Marangoni flow, resulting in the formation of a fully mixed cladding layer and a narrow transition zone at the bottom of the melt pool. However, this approach overlooks the influence of powder particle velocity, opting instead to simulate the impact of incident powder using a Gaussian mass source.

### 3.2. Cobalt-Based

Cobalt-based alloy cladding materials are well suited for equipment and parts requiring resistance to high temperatures, oxidation, abrasion, corrosion, and heat fatigue [91]. The strengthening mechanisms of these materials involve solid solution strengthening and precipitation strengthening [92]. The main strengthening alloying elements used in cobalt-based alloys are Co, Cr, W, Fe, Ni, and C [93,94]. The chemical compositions of cobalt-based powders for each study are shown in Table 5. Ni can lower the coefficient of thermal expansion of cobalt-based alloy fusion coatings, narrow the melting temperature range of the alloy, effectively enhance the fusion coating's crack-resistance sensitivity, and improve its wettability to the substrate [95]. Additionally, the dissolution of insoluble metal elements such as Cr, Mo, and W increases the lattice constants and impedes dislocation motion. Precipitation strengthening is highly dependent on the distribution, type, and size of carbides in the coating and serves as the primary mechanism for strengthening Co-based coatings [96,97].

Yue et al. [98] optimized the process parameters for Co-based alloy coatings. The findings indicated that the coating exhibited excellent adhesion to the substrate, with no visible cracks or voids. Furthermore, the cross-sectional area, aspect ratio, melting efficiency, and powder utilization of the melted track were enhanced by 4.065 mm<sup>2</sup>, 1.031, 19.032, and 70.3%, respectively. The optimal cladding track exhibited a strong bond with the substrate, free from cracks, holes, and noticeable element segregation.

**Table 5.** The cobalt-based powders of each study (mass fraction, wt.%).

| Materials  | C    | Si   | Mn   | Cr       | B    | Mo   | W     | Nb           | Fe   | Ni   | Co   | Ref. |
|------------|------|------|------|----------|------|------|-------|--------------|------|------|------|------|
| Co-based   | 1    | N/A  | N/A  | 5        | 13   | N/A  | N/A   | N/A          | 20   | N/A  | Bal. | [28] |
| Co-based   | 1    | N/A  | N/A  | 0, 5, 10 | 13   | N/A  | N/A   | N/A          | 10   | N/A  | Bal. | [29] |
| Co-based   | 1.0  | N/A  | N/A  | 5.0      | 12.0 | N/A  | N/A   | N/A          | 20.0 | N/A  | Bal. | [30] |
| Stellite-6 | 1.15 | 1.10 | 1.00 | 29.00    | N/A  | 1.00 | 4.50  | N/A          | 3.00 | 3.00 | Bal. | [36] |
| Co-based   | 1    | N/A  | N/A  | 5        | 10   | N/A  | N/A   | 0, 5, 15, 25 | 20   | N/A  | Bal. | [44] |
| Co-based   | 2.50 | 1.20 | 1.00 | 29.50    | N/A  | 1.00 | 12.50 | N/A          | 3.00 | 3.00 | Bal. | [98] |

### 3.3. Nickel-Based

Nickel is much cheaper than cobalt and also has excellent heat and corrosion resistance [99]. Hence, nickel-based alloy cladding materials are extensively utilized and predominate in numerous acidic and high-temperature environments [100]. The chemical compositions of each studied nickel-based powder are shown in Table 6. The alloying mechanisms of nickel-based alloys encompass solid solution strengthening of austenite by elements such as Cr and Fe [101], precipitation strengthening via synthesized intermetallic compounds of elements such as Fe and Ni [102], and strengthening of grain boundaries by elements such as B. In engineering applications, one or several reinforcement mechanisms are selected based on the specific performance design and application requirements.

**Table 6.** The nickel-based powders of each study (mass fraction, wt.%).

| Materials  | C       | Si      | Mn   | Cr       | Mo   | B       | Al      | W   | Cu  | Nb  | Fe        | Ti   | Co  | Ni   | Ref.     |
|------------|---------|---------|------|----------|------|---------|---------|-----|-----|-----|-----------|------|-----|------|----------|
| NiCrBSi    | 0.5–1.0 | 2.0–3.0 | N/A  | 9.0–12.0 | N/A  | 1.0–2.5 | 2.0–5.0 | N/A | N/A | N/A | ≤10       | N/A  | N/A | Bal. | [32]     |
| 58Ni 12Cr  | N/A     | N/A     | N/A  | 12       | 10   | 0.5     | N/A     | 9   | 4   | N/A | 4         | N/A  | N/A | 58   | [37]     |
| 10Mo 0.5B  | N/A     | N/A     | N/A  | 23       | 10   | N/A     | N/A     | N/A | N/A | 4   | N/A       | N/A  | N/A | 62   |          |
| 9W 4Cu 4Fe | N/A     | N/A     | N/A  | 12       | 5    | 1       | N/A     | N/A | N/A | N/A | 1         | N/A  | N/A | 76   |          |
| 62Ni 23Cr  | N/A     | 4       | N/A  | 12       | 5    | 1       | N/A     | N/A | N/A | N/A | 10.0      | N/A  | N/A | Bal. | [43]     |
| 10Mo 4Nb   | N/A     | 4       | N/A  | 12       | 5    | 1       | N/A     | N/A | N/A | N/A | 3.77      | N/A  | N/A | Bal. | [45]     |
| 76Ni 12Cr  | N/A     | 4       | N/A  | 12       | 5    | 1       | N/A     | N/A | N/A | N/A | 5.0       | N/A  | N/A | Bal. | [48]     |
| 5Mo 4Si 1B | N/A     | 4       | N/A  | 12       | 5    | 1       | N/A     | N/A | N/A | N/A | 3.62      | N/A  | N/A | Bal. | [52]     |
| 1Fe        | 0.45    | 3.0     | 0.2  | 13.0     | N/A  | 2.5     | N/A     | N/A | N/A | N/A | <8        | N/A  | N/A | Bal. | [54, 61] |
| Ni45       | 0.72    | 4.1     | 0.01 | 15.1     | 0.02 | 3.3     | N/A     | N/A | N/A | N/A | 0, 15, 30 | N/A  | N/A | Bal. | [56]     |
| NiCrBSi    | 0.7     | 4       | N/A  | 15       | N/A  | 3.2     | N/A     | N/A | N/A | N/A | 7.0–10.0  | N/A  | N/A | Bal. | [58]     |
| Ni60A      | 0.60    | 3.53    | N/A  | 7.52     | Bal. | 2.21    | N/A     | N/A | N/A | N/A | ≤4.2      | N/A  | N/A | Bal. | [60]     |
| Ni45       | 0.60    | 3.53    | N/A  | 7.52     | Bal. | 2.21    | N/A     | N/A | N/A | N/A | 11.61     | 0.56 | N/A | Bal. | [64]     |
| NiCrBSi    | 0.5–1.0 | 3.5–5.0 | N/A  | 14–19    | N/A  | 3.0–4.5 | N/A     | N/A | N/A | N/A |           |      |     |      |          |
| Ni-based   | 0.30    | 3.05    | N/A  | 7.01     | N/A  | 1.59    | N/A     | N/A | N/A | N/A |           |      |     |      |          |
| Ni60       | 0.5–1.0 | 3.5–5.0 | N/A  | 14–18    | N/A  | 3.0–4.5 | N/A     | N/A | N/A | N/A |           |      |     |      |          |
| NiCrBSi    | 0.68    | 3.4     | N/A  | 14       | N/A  | 3.4     | N/A     | N/A | N/A | N/A |           |      |     |      |          |
| Ni3Al      | N/A     | N/A     | 0.78 | N/A      | N/A  | 0.02    | 9.52    | N/A | N/A | N/A |           |      |     |      |          |

A. Ray et al. [37] employed three varieties of nickel-based powders containing varying amounts of Cr, Mo, B, and Nb as fusion cladding materials for laser fusion cladding. The objective was to improve the service life of side rolls subjected to high-temperature wear and corrosion. The results showed that the microstructures of the cladding layers were two-phase cellular dendritic structures in which the nickel-chrome dendrites between the interdendritic region were surrounded by hard precipitates. Hard precipitates enhance wear resistance, while the inclusion of chromium and molybdenum in the nickel-rich matrix enhances corrosion resistance. Powder materials exhibiting high wear resistance tend to enjoy prolonged service lives, particularly under weak corrosion conditions. Among the rolls tested, the coating with the highest boron and nickel content remained intact, whereas minor cracks and delaminations were observed on the surfaces of the other rolls.

### 3.4. High-Entropy Alloys

High-entropy alloys (HEAs) represent a class of metallic materials that have garnered significant interest in the field of materials science and engineering. It has been noted that during LC, rapid melting and variations in the diffusion rates of individual elements lead to compositional segregation, rendering the structure of non-HEAs incapable of



meeting design requirements [103,104]. Hence, the exploration of HEAs was prompted by their expansive range of compositional systems. Disparities in their compositions unavoidably yield notable differences in the matching process parameters of LC and post-treatment methods, thereby engendering a broad spectrum of microstructures and protective properties in the coatings [105].

Solid solution constitutes the primary-phase composition of HEAs; thus, the predominant form of strengthening is solid solution strengthening. Compared to traditional alloys, HEAs exhibit significantly enhanced specific strength, along with commendable wear resistance, corrosion resistance, high-temperature oxidation resistance, and comprehensive mechanical properties. Consequently, HEAs continue to be a vibrant area of research today [106,107].

HEAs are studied for coating the surface of 42CrMo steel using LC or plasma cladding [47,108,109]. Excellent performance can be achieved by adjusting the HEA material system. The shortcomings of 42CrMo steel can be compensated by this direction in the future.

### 3.5. Reinforcing Composite Coatings

Metal matrix composite coatings incorporating ceramic particles of tungsten carbide (WC) as reinforcing agents exhibit excellent strength, toughness, hardness, and wear resistance [110]. They find extensive applications in part protection, surface reinforcement, and worn part restoration, thereby playing a crucial role in extending part service life, reducing material consumption, and enhancing productivity [111]. Peng et al. [47] fabricated FeCoCrNi/WC coatings using both LC and plasma cladding (PC) methods. The findings revealed that the solid solution strengthening effect of element C was more pronounced in the PC coating. Moreover, the hardness of the HEA matrix in the LC coating was twice that of the PC coating, attributed to the robust retention of WC particles by LC, which exerted strong solidification force on the WC particles. Conversely, the PC coating exhibited a decrease in the retention force of the HEA matrix due to decarburization and oxidation of the WC particles.

The addition of rare earth oxides can effectively refine the reinforcing material within the coating, thereby enhancing its microstructure, reinforcing the tissue boundaries, and reducing defects [112–114]. The research of Cui et al. [115] supported this finding by preparing Co-based coatings containing CeO<sub>2</sub> on the surface of 42CrMo. This demonstrated that the addition of CeO<sub>2</sub> can significantly decrease the dilution rate of the coating, preventing the elements in Stellite-6 powder from diluting into the matrix. Additionally, CeO<sub>2</sub> was discovered to refine the grains within the coating, reduce the residual stress, and decrease the coating's crack sensitivity. Moreover, CeO<sub>2</sub> strengthened the internal structure of the coating, resulting in improved microhardness and wear resistance. Especially when the content of CeO<sub>2</sub> powder was 3 wt.%, the wear rate was merely half that of pure Stellite-6 coating, and the wear morphology appeared significantly smoother.

In summary, various materials possess unique strengthening mechanisms. Selecting the appropriate material depends on the specific scenario and the characteristics of the material.

## 4. Wear Resistance

In various industries, such as aerospace, mining, metallurgy, and other applications, surface wear of parts is a major cause of material failure. To solve this problem, wear-resistant coatings can be applied to the surface of the substrate. The wear resistance of the coating is improved by improving the composition, cracks, and inhomogeneities of the coating. In addition, the wear resistance can be improved by forming self-lubricating coatings. In the future, wear behavior can also be better studied by applying the finite element method to wear simulation [116]. Table 7 provides specific data on the improved wear resistance achieved.



#### 4.1. Improving Coatings

The inclusion of boron in coatings can enhance hardness and wear resistance by precipitating a high-hardness boride phase. For instance, the wear loss of LC iron-based coatings containing 0.75% boron is merely 10% of the wear observed in 42CrMo substrates [50]. Presently, boron additions are typically kept relatively low (<1.0 wt.%), and research has primarily focused on the impact of boron on carbide precipitates within coatings. However, there is a notable absence of systematic studies on coatings with high boron content, and the mechanism underlying the influence of boride morphology and distribution on coating wear resistance remains to be fully elucidated. Zhang et al. [42] investigated the effect of the B-Si ratio on the  $\text{Fe}_{10}\text{Co}_{10}\text{Ni}_{10}\text{Cr}_4\text{Mo}_6\text{B}_x\text{Si}_{10-x}$  LC layer. As depicted in Figure 4, a decrease in the B-Si ratio led to narrower worn tracks, attributed to heightened hardness resulting from an increased proportion of hard phases (BCC phase and  $\text{M}_x$  (B, Si)). In the absence of the B element, the wear mechanism of the  $\text{B}_0\text{Si}_{10}$  coating transitioned to serious abrasive wear. Notably, a white debris agglomerate, highlighted by a yellow circle in Figure 4e, was observed on the worn surface. The lowest friction coefficient (0.3786) and wear volume loss ( $2.46 \times 10^6 \mu\text{m}^3$ ) were recorded when  $x = 5$ , indicating that the  $\text{Fe}_{10}\text{Co}_{10}\text{Ni}_{10}\text{Cr}_4\text{Mo}_6\text{B}_5\text{Si}_5$  coating exhibited high toughness and optimal wear resistance. Furthermore, the study demonstrated that a single laser remelting once reduced compositional segregation in the coating, thereby enhancing its wear resistance. However, conducting two remeltings resulted in decreased hardness and wear resistance, attributed to the predominance of the FCC structure.

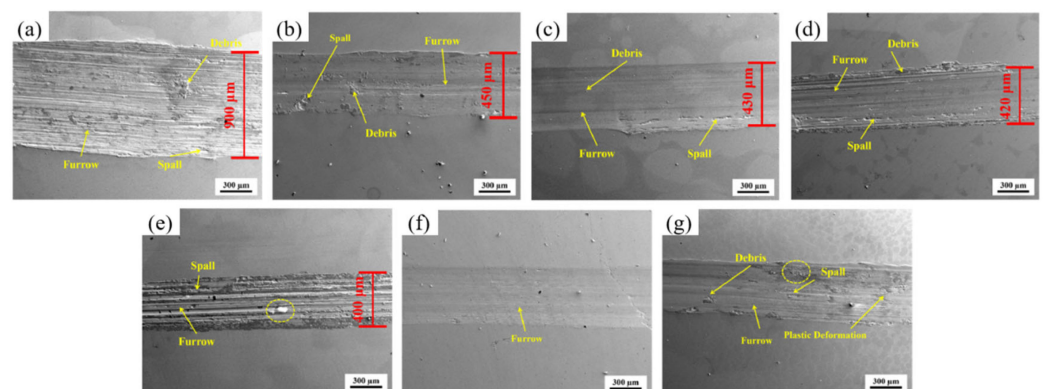


**Figure 4.** Worn morphologies of  $\text{Fe}_{10}\text{Co}_{10}\text{Ni}_{10}\text{Cr}_4\text{Mo}_6\text{B}_x\text{Si}_{10-x}$  coatings: (a)  $\text{B}_{10}\text{Si}_0$ ; (b)  $\text{B}_7\text{Si}_3$ ; (c)  $\text{B}_5\text{Si}_5$ ; (d)  $\text{B}_3\text{Si}_7$ ; (e)  $\text{B}_0\text{Si}_{10}$ ; (f) remelting once; (g) remelting twice [42].

Under high-temperature conditions, materials are prone to chemical changes, thermal expansion, and cracking, thereby increasing the risk of wear and failure [117]. Hence, investigating high-temperature wear resistance can aid in comprehending the wear resistance mechanism of materials in high-temperature environments and enhancing their durability and reliability. In high-temperature (500 °C) wear tests, N. Ur Rahman et al. [66] demonstrated that V-rich HSS, containing VC carbides, exhibited the most significant improvement in tribological properties. The predominant wear mechanism observed was oxidative wear. The high-temperature tribological properties of V-rich HSS rely on a blend of microstructural features and the average matrix carbide microhardness, with VC playing a crucial role in load-bearing capacity during wear. Similarly, two high-carbon HSS alloys,  $\text{Fe}_{\text{bal}}\text{-C-Cr-Mo-V}$  and  $\text{Fe}_{\text{bal-x}}\text{-C-Cr-Mo-V-W}_x$ , were used for LC coating treatment [34]. The microstructure of both alloys comprised a martensitic matrix with a network of primary and eutectic carbides. The latter demonstrated superior high-temperature wear resistance, attributed to a greater phase fraction of VC and  $\text{Mo}_2\text{C}$  carbides. Two types of Fe-Cr13-C alloys, one nitrogen-containing and the other non-nitrogen-containing, were utilized in the overlay. The nitrogen-containing overlay alloys exhibited superior high-temperature wear performance owing to the reinforcing effect of the carbon-nitride precipitates. In

high-temperature wear conditions, the finely dispersed and uniformly distributed carbonitrides precipitated within the matrix enhance abrasive wear resistance and diminish crack susceptibility [118].

Similarly, wear resistance can be further improved by heat treatment of laser-fused cladding. By heat treating the T15 LC coatings on the surface of 42CrMo steel, Zhang et al. [63] showed that the inhomogeneity of this coating could be effectively improved. This treatment resulted in a notable increase in the content of martensite and alloy carbide, consequently enhancing the resistance to abrasion. The predominant abrasion mechanisms observed in the fused cladding layer were abrasive wear and fatigue wear. Subsequent tempering treatment led to a marked decrease in the occurrence of cracks and shedding of the fused cladding layer. In contrast, the wear rate of 42CrMo steel after quenching was more than three times higher compared to that of the untreated T15 coating. In both cases, abrasive wear, fatigue cracking, and spalling of the T15 layer were evident [53].

As previously stated, the role of rare earth oxides in the material involves refining the coating grain, enhancing the microstructure of the coating, strengthening organizational boundaries, and reducing flaws, all of which increase wear resistance [119]. Qi et al. [39] used LC to prepare Fe55 + 10 wt.% nano TiC + 1 wt.% nano CeO<sub>2</sub> coatings on the surface of 42CrMo steel, which exhibited optimal wear performance. The size, morphology, and dispersion of TiC particles were influenced by the content of nano TiC, which also eliminated macroscopic defects in the coating. One crucial way of research for enhancing the wear resistance of coatings involves temperature field control to regulate the morphology of TiC particles and other phases. Moreover, incorporating TiO<sub>2</sub> nanoparticles into the cladding material can enhance the wear resistance of the hard cladding layer by promoting microstructure uniformity and augmenting carbide presence [22].

#### 4.2. Self-Lubricating Coatings

The anti-friction properties of coatings are often unsatisfactory due to the high hardness of hard coatings during friction, leading to accelerated wear of the counterparts. To address this issue, researchers have developed self-lubricating coatings by adding solid lubricants to hard coatings, thereby enhancing their lubricating properties. Solid self-lubricating technology mitigates the shortcomings of conventional lubricants and greases in severe-usage environments, making it increasingly prevalent for achieving anti-wear and wear-resistance functionalities in metallic mechanical parts, particularly under high-temperature and heavy-load conditions [120–124]. Liu et al. [43] utilized LC to study the performance of Ni-coated graphite composite powder and Ni45 alloy powder when applied to 42CrMo steel. The results revealed that the Ni cladding could effectively shield the ablation of graphite and slowed down the reaction between carbon and other components. By employing a scanning speed of 300 mm/s, a Ni-based self-lubricating coating with desirable attributes such as low porosity, uniform microstructure, moderate hardness, low friction coefficient, and minimal wear rate was successfully synthesized. Its average friction coefficient and wear volume were about 0.480 and  $6.824 \times 10^{-6} \text{ mm}^3 \cdot \text{N}^{-1} \cdot \text{m}^{-1}$ , respectively. The predominant wear mechanisms observed were slight abrasive wear and adhesive wear.

In recent years, SnAgCu multi-solid lubricants have been proven to segregate into a low-friction lubricating film at the interface of the alloy during the friction process [125]. Liu et al. [126] formed an ordered microporous nickel-based hard coating structure with the solid lubricant SnAgCu in the micropits of the 42CrMo surface. The preparation process flow is depicted in Figure 5a. Figure 5b is a schematic representation of the mechanism for anti-friction and wear resistance. During friction at medium and high temperatures, the lubricant SnAgCu within the micro-pits of the nickel-based hard coating surface gradually diffuses onto the worn surface, forming a lubrication layer with low shear ability. This layer, rich in lubricant SnAgCu and oxides, significantly reduces friction. Moreover, nanocrystals present on the hard coating surface enhance its strength and wear resistance. Additionally, the flow behavior of SnAgCu on the worn surface serves to repair microcracks and safeguard the coating from damage. Compared to the substrate, the wear

rate and friction coefficient were reduced by more than 20% and 35%, respectively, across the temperature range of 25–400 °C.

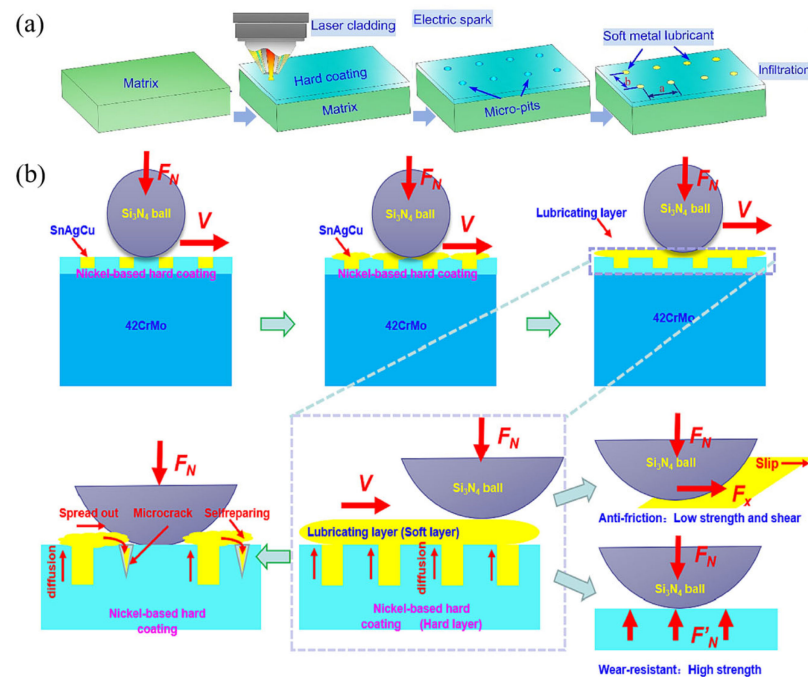


**Figure 5.** (a) Schematic diagram of the preparation process of the ordered microporous wear-resistant self-lubricating integrated material; (b) schematic diagram of the anti-friction and wear-resistance mechanism [126].

In conclusion, the wear-resistance mechanism of the 42CrMo steel surface coating is shown in Figure 6. The wear resistance of the coating is improved by improving the carbides, nitrides, and borides in the coating, among which the carbides have the greatest influence on the wear resistance of the coating, as shown in Figure 6a. Coating defects such as cracks and nonuniformities are improved by selecting suitable process methods and process parameters, as shown in Figure 6c. Self-lubricating coatings are formed by solid lubricants (CaF<sub>2</sub>, h-BN, MoS<sub>2</sub>, WS<sub>2</sub>, Ag, etc.). Meanwhile, the self-lubricating coating can compensate for the defects in the coating, as shown in Figure 6b. The above wear-resistance mechanisms may work individually or with two or three at the same time.

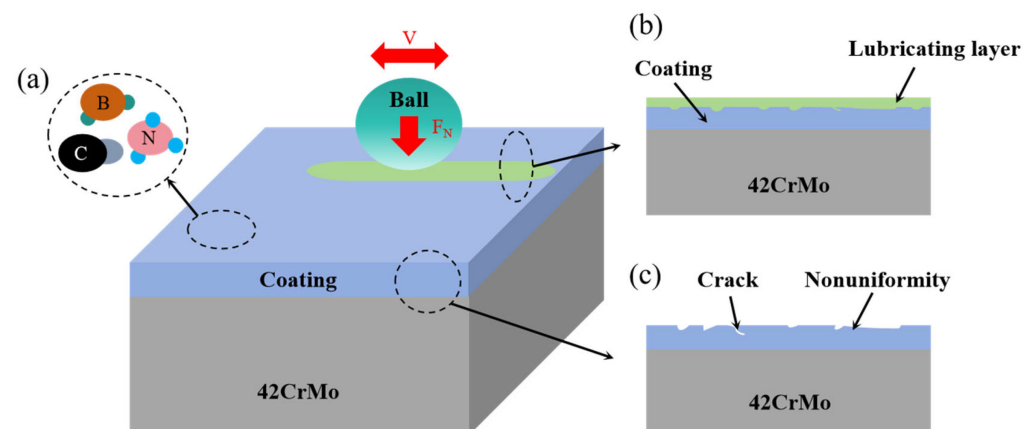


**Figure 6.** The 42CrMo steel surface coating wear resistance mechanism: (a) improving the compounds of the coating; (b) lubricating layer; (c) improving the coating defects.

Table 7. Comparative experimental data on the wear resistance of 42CrMo steel surface coatings.

| Technology                            | Materials  | Counterpart                    | Parameters                       | Temperature                                       | Mode                           | COF   | Wear Loss  | Mechanism                          | Ref.  |
|---------------------------------------|--|--------------------------------|----------------------------------|---|--------------------------------|---|--|------------------------------------|-------|
| High-velocity oxygen fuel spraying    | WC-12%Cr <sub>3</sub> C <sub>2</sub> -6%Ni   | Si <sub>3</sub> N <sub>4</sub> | 560 r/s;<br>10 N                 | 25 °C;<br>450 °C;<br>600 °C;<br>750 °C;<br>800 °C | Dry sliding                    | (Unsealed)<br>25 °C: 0.31 ± 0.03;<br>450 °C: 0.41 ± 0.02;<br>600 °C: 0.59 ± 0.01;<br>750 °C: 0.48 ± 0.03;<br>800 °C: 0.71 ± 0.02;<br>(Sealed)<br>25 °C: 0.24 ± 0.01;<br>450 °C: 0.38 ± 0.03;<br>600 °C: 0.48 ± 0.02;<br>750 °C: 0.51 ± 0.02;<br>800 °C: 0.65 ± 0.01 | N/A  | Contact fatigue and oxidative wear | [11]  |
| Plasma spraying + Induction remelting | NiCrBSi+Ti   | N/A                            | 30 min;<br>200 rad/min;<br>300 N | N/A   | Sliding                        | NiCrBSi-TiN: 0.63;<br>Induction remelting: 0.59   | N/A  | N/A                                | [15]  |
| Deposition                            | 30 g/L CoSO <sub>4</sub> ·7H <sub>2</sub> O,<br>30 g/L NiSO <sub>4</sub> ·6H <sub>2</sub> O,<br>80 g/L C <sub>6</sub> H <sub>5</sub> Na <sub>3</sub> O <sub>7</sub> ,<br>20 g/L Na <sub>2</sub> SO <sub>4</sub> ,<br>30 g/L H <sub>3</sub> BO <sub>3</sub> | N/A                            | 3 mm;<br>20 min;<br>10 N         | N/A   | Simulated gear oil environment | N/A   | NaH <sub>2</sub> PO <sub>2</sub> concentration 0, 5, 10, 15, 20 (g/L)<br>Depth and width:<br>5.08, 542.86;<br>2.86, 428.57;<br>2.07, 328.24;<br>1.35, 257.14;<br>2.05, 314.19 (µm) | N/A                                | [17]  |
| Hardfacing                            | N, CrN, Nb, Ti   | Carbon steel                   | 45 min;<br>50 m/min;<br>600 N    | 600 °C  | Sliding                        | N/A   | H1: 0.045 g;<br>H2: 0.056 g  | Abrasive wear                      | [118] |
| LC                                    | Fe-based   | GCr15                          | 30 min;<br>200 rpm;<br>30 kgf    | 20 °C   | Sliding                        | N/A   | 9–10 mg  | N/A                                | [27]  |
| LC                                    | 3540 Fe, CeO <sub>2</sub>  | Al <sub>2</sub> O <sub>3</sub> | 5 N                              | N/A   | Sliding                        | Without ultrasonic vibration: 0.52;<br>45°: 0.26;<br>90°: 0.4   | N/A  | Adhesive wear                      | [31]  |

Table 7. Cont.

| Technology | Materials   | Counterpart                    | Parameters   | Temperature           | Mode        | COF                  | Wear Loss   | Mechanism   | Ref. |
|------------|---|--------------------------------|--|-----------------------|-------------|----------------------|---|---|------|
| LC         | NiCrBSi   | Si <sub>3</sub> N <sub>4</sub> | 20 min;<br>5 mm;<br>20 N                                     | N/A                   | Sliding     | N/A                  | No auxiliary field:<br>0.0077; 0.0088; 0.0110;<br>Electromagnetic and<br>ultrasonic field assist:<br>0.0062; 0.0073; 0.0093<br>(mm <sup>3</sup> )                               | Slight adhesive<br>and abrasive<br>wear   | [32] |
| LC         | HSS   | Low-carbon<br>steel disc       | 2000 m;<br>0.45 m/s;<br>5 N                                  | 500 °C                | Sliding     | X1: 0.55<br>X2: 0.60 | X1: 4.215;<br>X2: 3.418<br>( $\times 10^{-5}$<br>mm <sup>3</sup> ·N <sup>-1</sup> ·m <sup>-1</sup> )  | Adhesive and<br>oxidative wear  | [34] |
| LC         | Fe-based  | Al <sub>2</sub> O <sub>3</sub> | 180 min;<br>200 r/min;<br>100 N                              | N/A                   | Sliding     | N/A                  | $0.92 \times 10^{-5}$<br>mm <sup>3</sup> ·N <sup>-1</sup> ·m <sup>-1</sup>  | Micro-cutting<br>and slight<br>oxidative wear   | [35] |
| LC         | HSS   | Low-carbon<br>steel discs      | 2000 m;<br>450 mm/s;<br>5 N                                  | 25 °C, 500<br>°C      | Sliding     | N/A                  | 25 °C:<br>LC1: 1.68<br>LC2: 0.65<br>LC3: 0.67<br>500 °C:<br>LC1: 44.63<br>LC2: 46.19<br>LC3: 27.19<br>( $\times 10^{-5}$<br>mm <sup>3</sup> ·N <sup>-1</sup> ·m <sup>-1</sup> ) | The combined<br>effect of<br>abrasive,<br>adhesion, and<br>frictional<br>oxidative wear | [38] |
| LC         | Fe55 + nano-TiC<br>+ nano-CeO <sub>2</sub>  | Al <sub>2</sub> O <sub>3</sub> | 60 min;<br>8 mm;<br>70 mm/min;<br>20 N                       | 25 °C                 | Sliding     | FT2: 0.6897          | FT2: 1.99143;<br>FTC1: 1.685221<br>( $\times 10^{-2}$ mm <sup>3</sup> )   | N/A   | [39] |
| LC         | CuPb <sub>10</sub> Sn <sub>10</sub>   | Si <sub>3</sub> N <sub>4</sub> | 1300 rpm;<br>700 g<br>30 min;<br>5 mm;<br>10 mm/min;<br>30 N | 15 °C                 | Dry sliding | 0.19                 | 12.1 mm <sup>3</sup>  | N/A   | [41] |
| LC         | Fe <sub>10</sub> Co <sub>10</sub> Ni <sub>10</sub> Cr <sub>4</sub><br>Mo <sub>6</sub> B <sub>x</sub> Si <sub>10-x</sub> | ZrO <sub>2</sub>               |  | Room tem-<br>perature | Sliding     | x = 5: 0.3786        | x = 5: $2.46 \times 10^6$ µm <sup>3</sup>   | N/A   | [42] |



Table 7. Cont.

| Technology | Materials   | Counterpart                    | Parameters                                     | Temperature      | Mode        | COF  | Wear Loss  | Mechanism   | Ref. |
|------------|-------------|--------------------------------|--|------------------|-------------|--|--|---|------|
| LC         | Ni45, Gr/Ni | GCr15                          | 30 min;<br>400 r/min;<br>98 N                  | Room temperature | Dry sliding | N/A  | 200, 300, 400<br>(mm/min): 1.72; 1.26;<br>1.7<br>(mm <sup>3</sup> );<br>9.136; 6.824; 9.208<br>( $\times 10^{-6}$<br>mm <sup>3</sup> ·N <sup>-1</sup> ·m <sup>-1</sup> ) | Slight abrasive<br>and adhesive<br>wear           | [43] |
| LC         | Co-based    | Si <sub>3</sub> N <sub>4</sub> | 30 min;<br>2 Hz;<br>20 N                       | N/A              | Sliding     | C1–C8: 0.58; 0.56; 0.60;<br>0.55; 0.72; 0.65; 0.56; 0.63 | N/A  | N/A   | [44] |
| LC         | WC + Co06   | GCr15                          | 3600 s;<br>5 Hz;<br>100 N                      | Room temperature | Dry sliding | N/A  | 0.0617 mm <sup>3</sup>   | N/A   | [46] |
| LC         | HSS         | Al <sub>2</sub> O <sub>3</sub> | 180 min;<br>200 r/min;<br>100 N                | Room temperature | Dry sliding | N/A  | S4: 0.0965 g;<br>S1: 0.4857 g  | N/A   | [50] |
| LC         | Ni45, Mo    | GCr15                          | 30 min;<br>200 rev/min;<br>294 N               | 20 °C            | Sliding     | N/A  | Ni45 + 10%Mo: 8 mg;<br>Ni45: 14 mg   | N/A   | [52] |
| LC         | T15         | YG6                            | 120 min;<br>1.67;<br>20 N, 30 N, 50 N,<br>70 N | N/A              | Sliding     | N/A  | 20N: 0.78;<br>70N: 0.58<br>( $\times 10^{-6}$<br>mm <sup>3</sup> ·N <sup>-1</sup> ·m <sup>-1</sup> )   | Abrasive wear,<br>fatigue cracks,<br>and spalling | [53] |
| LC         | NiCrBSi     | GCr15                          | 30 min;<br>200 rev/min;<br>300 N               | N/A              | Sliding     | N/A  | 1500 W: 7.5;<br>2000 W: 6;<br>2500 W: 8.5;<br>3000 W: 10.5;<br>3500 W: 13.2<br>(mg)  | N/A   | [54] |
| LC         | NiCrBSi     | Si <sub>3</sub> N <sub>4</sub> | 50 min;<br>2 Hz;<br>100 N                      | N/A              | Sliding     | N/A  | No.1–No.9: 0.0067;<br>0.0176; 0.0112; 0.0176;<br>0.0227; 0.0234; 0.0143;<br>0.0244; 0.0209<br>(mm <sup>3</sup> )   | N/A   | [55] |

Table 7. Cont.

| Technology | Materials   | Counterpart                        | Parameters   | Temperature           | Mode        | COF | Wear Loss   | Mechanism   | Ref. |
|------------|---|------------------------------------|--|-----------------------|-------------|-----|---|---|------|
| LC         | Different Co contents<br>Ni-based alloy   | GCr15                              | 30 min;<br>200 r/min;<br>300 N                       | 20 °C                 | Sliding     | N/A | 0 wt.% Co: 24;<br>15 wt.% Co: 13;<br>30 wt.% Co: 7<br>(mg)  | From abrasive wear to adhesive wear with the increase of Co content | [56] |
| LC         | Ni60 +<br>nano-WC +<br>CeO <sub>2</sub>   | GR<br>(4Cr3Mo3W4VNb)<br>steel ball | 20 min;<br>10 Hz;<br>500 rpm;<br>19.8 N              | 400 °C                | Sliding     | N/A | 0%, 0.5%, 1.0%, 1.5%,<br>2.0% CeO <sub>2</sub> : 10.7; 8.4;<br>6.1; 15.5; 17.2<br>(mg)<br>(50 mm/s)<br>5500 W, 5000 W, 4000<br>W, 3000 W: 3.08, 3.38,<br>3.14, 12.82;<br>(3000 W) | Abrasive wear, slight adhesive wear                                 | [58] |
| LC         | Synthetic<br>diamond, Ti, Ni,<br>Fe <sub>24.1</sub> Co <sub>24.1</sub> Cr <sub>24.1</sub><br>Ni <sub>24.1</sub> Mo <sub>3.6</sub><br>(at.%) | Si <sub>3</sub> N <sub>4</sub>     | 15 min;<br>5 mm;<br>50 Hz;<br>900 times/min;<br>50 N | N/A                   | Sliding     | N/A | 40, 50 mm/s: 3.98,<br>12.82<br>(Diamond content)<br>5 wt.%, 10 wt.%, 15<br>wt.%, 20 wt.%. 12.82,<br>15.48, 18.19, 16.63<br>(mm <sup>2</sup> )                                     | N/A   | [59] |
| LC         | NiCrBSi   | GCr15                              | 30 min;<br>500 r/min;<br>300 N                       | Room tem-<br>perature | Dry sliding | N/A | 0.3 mg  | N/A   | [60] |
| LC         | T15   | YG6                                | 120 min;<br>120 m;<br>5 mm;<br>100 r/min;<br>50 N    | Room tem-<br>perature | Dry sliding | N/A | CA: 7.3<br>HAZ: 4.3<br>Quenching: 5.6<br>Quenching-<br>tempering: 8.5<br>( $\times 10^{-7}$<br>mm <sup>3</sup> ·N <sup>-1</sup> ·m <sup>-1</sup> )                                | Abrasive and fatigue wear   | [63] |

Table 7. Cont.

| Technology             | Materials   | Counterpart                    | Parameters                         | Temperature                                       | Mode        | COF      | Wear Loss   | Mechanism   | Ref.  |
|------------------------|---|--------------------------------|------------------------------------|---|-------------|----------|---|---|-------|
| LC                     | Cr <sub>7</sub> C <sub>3</sub> /Ni <sub>3</sub> Al;<br>Cr <sub>3</sub> C <sub>2</sub> /Ni <sub>3</sub> Al | Gray cast iron                 | 60 min;<br>200 r/min;<br>30 N      | Room tem-<br>perature                             | Dry sliding | N/A      | Cr <sub>7</sub> C <sub>3</sub> /Ni <sub>3</sub> Al:<br>0.82 ± 0.05;<br>Cr <sub>3</sub> C <sub>2</sub> /Ni <sub>3</sub> Al:<br>1.42 ± 0.05<br>(mg)   | Cr <sub>7</sub> C <sub>3</sub> /Ni <sub>3</sub> Al:<br>Abrasive wear<br>Cr <sub>3</sub> C <sub>2</sub> /Ni <sub>3</sub> Al:<br>Abrasive and<br>micro-adhesive<br>wear | [64]  |
| LC                     | Fe-based  | Si <sub>3</sub> N <sub>4</sub> | 30 min;<br>2 mm;<br>10 Hz;<br>50 N | Room tem-<br>perature                             | Dry sliding | N/A      | 1.2466151 × 10 <sup>7</sup> μm <sup>3</sup>   | N/A   | [65]  |
| LC                     | V-rich HSS  | Low-carbon<br>steel discs      | 2000 m;<br>0.45 m/s;<br>5 N        | 500 °C  | Sliding     | 0.55-0.6 | 5V: 19.34;<br>10V: 21.73;<br>15V: 30.1<br>(×10 <sup>-6</sup><br>mm <sup>3</sup> ·N <sup>-1</sup> ·m <sup>-1</sup> )<br>M: 25 °C: 2.5;<br>200 °C: 3.4;<br>300 °C: 2.6;<br>400 °C: 4.1;<br>MC: 400 °C: 2.6;<br>MCS: 25 °C: 1.9;<br>300 °C: 1.2;<br>400 °C: 2.0<br>(×10 <sup>-6</sup><br>mm <sup>3</sup> ·N <sup>-1</sup> ·m <sup>-1</sup> ) | Abrasive,<br>adhesive, and<br>oxidative wear  | [66]  |
| LC                     | Ni60, SnAgCu  | Si <sub>3</sub> N <sub>4</sub> | 0.2 m/s;<br>8 N                    | 25 °C,<br>100 °C,<br>200 °C,<br>300 °C,<br>400 °C | Sliding     | N/A      | LC: 0.7;<br>PC: 8.29<br>(×10 <sup>-5</sup><br>mm <sup>3</sup> ·N <sup>-1</sup> ·m <sup>-1</sup> )   | N/A   | [126] |
| LC; Plasma<br>cladding | Fe <sub>25</sub> Co <sub>25</sub> Cr <sub>25</sub> Ni <sub>25</sub><br>(in at.%)                          | SiC                            | 9 m/min;<br>50 N                   | Room tem-<br>perature                             | Sliding     | N/A      | LC: 0.7;<br>PC: 8.29<br>(×10 <sup>-5</sup><br>mm <sup>3</sup> ·N <sup>-1</sup> ·m <sup>-1</sup> )   | LC: Abrasive<br>wear<br>PC: Adhesion<br>wear  | [47]  |
| Nitriding              | Ti  | GCr15                          | 15 min;<br>200 rpm;<br>400 g       | N/A   | Sliding     | 0.32     | N/A   | N/A   | [2]   |
| Nitriding              | Al (NO <sub>3</sub> ) <sub>3</sub>  | GCr15                          | 15 min;<br>214 r/min;<br>200 g     | N/A   | Sliding     | 0.29     | 1.21 × 10 <sup>-5</sup><br>g·m <sup>-1</sup> ·N <sup>-1</sup>   | N/A   | [76]  |

Table 7. Cont.

| Technology                  | Materials   | Counterpart                    | Parameters   | Temperature      | Mode        | COF                  | Wear Loss  | Mechanism | Ref.  |
|-----------------------------|---|--------------------------------|--|------------------|-------------|----------------------|--|-----------|-------|
| Nitriding                   | CuSO <sub>4</sub> + NaOH  | GCr15                          | 5 mm;<br>60 min;<br>10 mm/s;<br>1200 rpm;<br>2 N, 10 N | Room temperature | Dry sliding | N/A                  | 51 µm  | N/A       | [127] |
| Nitriding                   | PN  | GCr15                          | 16 min;<br>250 r/min;<br>400 g                         | N/A              | Sliding     | N/A                  | 1.02 mg/cm <sup>2</sup>  | N/A       | [128] |
| Plasma cladding             | WC +<br>Fe <sub>25</sub> Co <sub>25</sub> Cr <sub>25</sub> Ni <sub>25</sub> | Si <sub>3</sub> N <sub>4</sub> | 9 m/min;<br>50 N                                       | Room temperature | Sliding     | N/A                  | Spherical WC: 3.27;<br>Irregular WC: 8.13<br>( $\times 10^{-7}$<br>mm <sup>3</sup> ·N <sup>-1</sup> ·m <sup>-1</sup> )                         | N/A       | [108] |
|                             |   |                                |  |                  |             | N/A                  | 10%WC: 303;<br>60%WC: 3.27;<br>70%WC: 8.57<br>( $\times 10^{-7}$<br>mm <sup>3</sup> ·N <sup>-1</sup> ·m <sup>-1</sup> )                        |           | [109] |
| Vacuum fusion               | Diamond grits +<br>NiCrBSi  | GCr15                          | 10 mm;<br>30 min;<br>2 Hz;<br>50 N                     | Room temperature | Sliding     | I: 0.60;<br>II: 0.47 | N/A  | N/A       | [129] |
| Electric arc ion<br>plating | Cr/CrN +<br>TiAlSiN   | N/A                            | 120 min;<br>0.2 m/s;<br>1000 g                         | N/A              | Sliding     | N/A                  | 10V: 2.64;<br>20V: 2.31;<br>30V: 1.91;<br>40V: 3.24;<br>50V: 4.16<br>( $\times 10^{-5}$<br>mm <sup>3</sup> ·N <sup>-1</sup> ·m <sup>-1</sup> ) | N/A       | [130] |

## 5. Corrosion Resistance

Corrosion is a common cause of failure in metallic materials, especially steel [131]. A comparison of the improved corrosion properties under specific corrosive environments is shown in Table 8. The formation of a corrosion-resistant coating on the surface of 42CrMo steel, the improvement of defects existing in some coatings, and the production of a dense passivation film on the surface of the coating can effectively prevent the entry of corrosive ions, thus preventing 42CrMo steel from being corroded.

### 5.1. Corrosion-Resistant Coatings

A 42CrMo steel can be effectively protected by forming a corrosion-resistant coating on its surface. Kang et al. [76] deposited an aluminum hydroxide film on the surface of 42CrMo steel by utilizing electrolytic aluminum nitrate prior to nitriding. This process led to a significant enhancement in corrosion resistance, attributed to the formation of a hybrid compound in the surface layer. In comparison to conventional plasma nitriding, the corrosion current decreased from  $9.23 \times 10^{-7} \text{ A/cm}^2$  to  $2.20 \times 10^{-7} \text{ A/cm}^2$ , while the corrosion potential increased from  $-605.30 \text{ mV}$  to  $-299.58 \text{ mV}$ . Furthermore, the corrosion rate witnessed a substantial decrease from  $5.42 \text{ } \mu\text{m/A}$  to  $1.23 \text{ } \mu\text{m/A}$ . Zhang et al. [18] utilized chemical vapor deposition to fabricate TiC/Ti(CN)/TiN multilayer coatings, aiming to enhance surface protection for high-strength steels exposed to challenging, corrosive hydrogen sulfide environments. This innovative coating significantly mitigated corrosion rates, reducing them by at least 50 times compared to the untreated substrate while also demonstrating impressive resistance to chloride ion corrosion. Furthermore, the presence of high-strength steel substrates exerted a notable promotional effect against hydrogen sulfide stress corrosion cracking. Remarkably, even after exposure to corrosive conditions, the coating retained its exceptional hardness properties. This helped the coating to show good service life in harsh environments.

### 5.2. Improving Defects and Microstructure

Corrosion resistance can be improved by modifying the macroscopic defects and microstructure of 42CrMo steel surface coatings. Rare earth Y modification to enhance corrosion resistance is attributed to the following reasons: Y can refine the crystalline particles and minimize defects. Y exhibits a strong affinity for impurity elements (O, H, etc.), facilitating the formation of stable compounds and reducing the presence of impurities in the coating. Liu et al. [132] prepared Zn-Fe and Y-modified Zn-Fe coatings on 42CrMo steel using the LC technique. Their findings revealed that Y modification decreased the activation energy and significantly improved corrosion resistance. The corrosion area of the Y-modified Zn-Fe coating was notably smaller compared to the standard Zn-Fe coating, as depicted in Figure 7. Corrosion predominantly occurred at coating defects, such as minor cracks and holes, with only minor corrosion pits observed on the surface of the Y-modified Zn-Fe coatings. In addition, the  $E_{\text{corr}}$  of the Zn-Fe coating was more negative than that of the Y-modified Zn-Fe coating, and the  $i_{\text{corr}}$  of the Zn-Fe coating was significantly larger than that of the Y-modified Zn-Fe coating. In summary, these findings underscore the superior NaCl corrosion resistance of Y-modified Zn-Fe coatings compared to conventional Zn-Fe coatings.

Sun et al. [9] demonstrated that the impact of heat treatment temperature on the corrosion resistance of coatings could be attributed to three factors: the internal stress state, the microstructure and phase structure of the bonded phases, and, most critically, the original presence of pores and cracks. They investigated the effect of heat treatment on the corrosion performance of WC-17Co coatings prepared by LC. The order of corrosion resistance for the coatings in the sprayed and heat-treated states in 5 wt.%  $\text{H}_2\text{SO}_4$  solution was as follows:  $500^\circ\text{C} > 900^\circ\text{C} > \text{sprayed state} > 700^\circ\text{C} > 1100^\circ\text{C}$ . Different discontinuous flaky oxide films formed on the surface of the heat-treated coatings, indicating that the binder structure significantly influenced the corrosion resistance of the coatings.



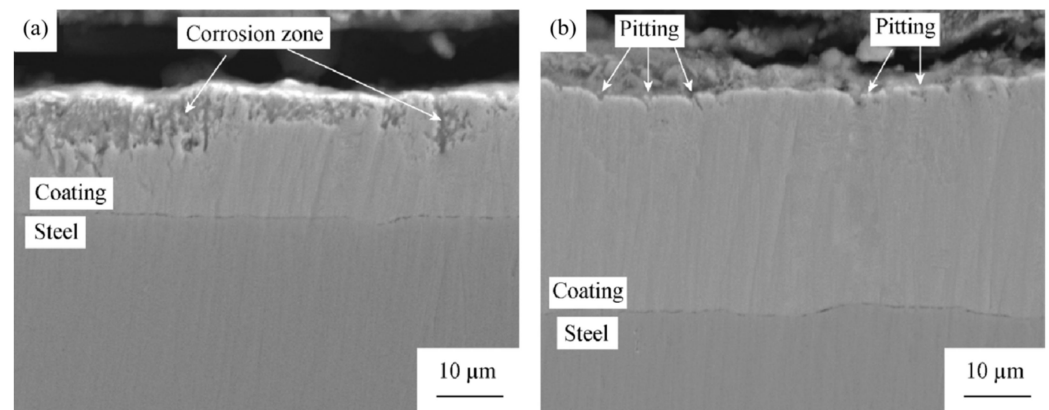


**Figure 7.** (a) Zn-Fe coating; (b) Y-modified Zn-Fe coating [132].

### 5.3. Passivation Film

A dense passivation film is produced on the surface of the coating, which effectively prevents corrosive ions from entering the coating and the substrate. WC improves corrosion resistance by forming a passivation film on the surface of the LC coating. A spherical WC-reinforced nickel-based composite coating was prepared on 42CrMo steel. This led to the formation of a stable and dense passivation film, which effectively slowed down the corrosion of the substrate in the HCl solution [100,133]. During immersion tests, intense pit corrosion and consumption of the Ni matrix were induced by micro-galvanic reactions occurring at the interfaces of newly formed phases and the Ni matrix. With prolonged immersion time, observable debonding between Ni-rich and W-rich phases occurred. Compared to atmospheric pressure conditions, elevated  $\text{Cl}^-$  activity under pressure facilitated heightened adsorption and penetration of  $\text{Cl}^-$  on the coating surface, consequently diminishing its corrosion resistance. These discoveries carry significant implications for the practical application of the coating.

Coatings are enriched with Cr elements to produce passivated films for improved corrosion resistance [134]. Cui et al. [49] prepared a multi-pass Stellite-6 coating on the surface of 42CrMo steel using the LC technique. The presence of dense passivation film, induced by the Cr-rich elemental dendrites, contributed to enhanced corrosion resistance in the overlapped zone compared to the non-overlapped zone. Additionally, the smaller equiaxed crystals facilitated the formation of more active sites for the generation of passivation film ( $\text{Cr}_2\text{O}_3$ ), consequently retarding the corrosion process induced by  $\text{Cl}^-$ . Cui et al. [36] investigated the effect of LC process parameters ( $L_{\text{ed}} = 64\text{--}100 \text{ J/mm}^2$ ) ( $L_{\text{ed}}$ : laser power/(scanning speed  $\times$  spot diameter)) on the corrosion resistance of Co-based coatings (97 wt.% Stellite-6 and 2 wt.%  $\text{CeO}_2$ ). They observed that initially, the corrosion resistance of the coatings increased with the  $L_{\text{ed}}$  content but later decreased. Moreover, a dense passivation film formed on the coatings' surface, resulting in a low corrosion current density of only  $1.740 \times 10^{-7} \text{ (A/cm}^2\text{)}$  under appropriate process parameters.

To summarize, the mechanism of improving the corrosion resistance of 42CrMo steel is shown in Figure 8. A 42CrMo steel can be effectively protected by applying corrosion-resistance coatings to the surface of the substrate using the previously mentioned techniques. Coatings may include defects that diminish their corrosion resistance. Coating grain refinement and the reduction of defects and impurities can be achieved through the addition of rare earths, process optimization, or post-treatment. Due to the role of certain elements (such as Cr, WC, etc.), a dense passivation film can be produced on the surface of the coating, effectively preventing the entry of corrosive ions and thereby preventing the coating and the substrate from being corroded.

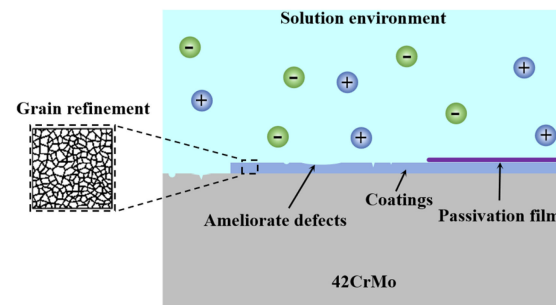


**Figure 8.** Schematic diagram of the corrosion resistance mechanism of 42CrMo steel.

**Table 8.** Effect of different material system coatings on the surface of 42CrMo steel on corrosion resistance.

| Technology                         | Materials   | Corrosive Medium Solution      | Electrochemical Parameters of the Substrate |  | Electrochemical Parameters of Coatings |  | Ref.  |
|------------------------------------|---|--------------------------------|---|--|--|--|-------|
|                                    |   |                                | $E_{corr}$ (mV)                             | $i_{corr}$ ( $\mu\text{A}/\text{cm}^2$ ) | $E_{corr}$ (mV)                        | $i_{corr}$ ( $\mu\text{A}/\text{cm}^2$ ) |       |
| High-velocity oxygen fuel spraying | WC-17Co   | 5 wt.% $\text{H}_2\text{SO}_4$ | N/A   | N/A                                      | C-A: −118                              | C-A: 1                                   | [9]   |
| High-velocity oxygen fuel spraying | WC-17Co   | 5 wt.% $\text{H}_2\text{SO}_4$ | N/A   | N/A                                      | C-5: −17                               | C-5: 0.1                                 | [9]   |
| High-velocity oxygen fuel spraying | WC-17Co   | 5 wt.% $\text{H}_2\text{SO}_4$ | N/A   | N/A                                      | C-7: −138                              | C-7: 1.99                                | [9]   |
| High-velocity oxygen fuel spraying | WC-17Co   | 5 wt.% $\text{H}_2\text{SO}_4$ | N/A   | N/A                                      | C-9: −78                               | C-9: 0.40                                | [9]   |
| High-velocity oxygen fuel spraying | WC-17Co   | 5 wt.% $\text{H}_2\text{SO}_4$ | N/A   | N/A                                      | C-11: −143                             | C-11: 3.98                               | [9]   |
| High-velocity oxygen fuel spraying | WC-12%Cr <sub>3</sub> C <sub>2</sub> -6%Ni              | 3.5 wt.% NaCl                  | N/A   | N/A                                      | T1: −509                               | T1: 2.0                                  | [10]  |
| High-velocity oxygen fuel spraying | WC-12%Cr <sub>3</sub> C <sub>2</sub> -6%Ni              | 3.5 wt.% NaCl                  | N/A   | N/A                                      | T2: −468                               | T2: 8.9                                  | [10]  |
| High-velocity oxygen fuel spraying | WC-12%Cr <sub>3</sub> C <sub>2</sub> -6%Ni              | 1 mol/L HCl                    | N/A   | N/A                                      | T1: −486                               | T1: 1.8                                  | [10]  |
| High-velocity oxygen fuel spraying | WC-12%Cr <sub>3</sub> C <sub>2</sub> -6%Ni              | 1 mol/L HCl                    | N/A   | N/A                                      | T2: −408                               | T2: 1.6                                  | [10]  |
| High-velocity oxygen fuel spraying | WC-12%Cr <sub>3</sub> C <sub>2</sub> -6%Ni              | 1 mol/L NaOH                   | N/A   | N/A                                      | T1: −464                               | T1: 2.5                                  | [10]  |
| High-velocity oxygen fuel spraying | WC-12%Cr <sub>3</sub> C <sub>2</sub> -6%Ni              | 1 mol/L NaOH                   | N/A   | N/A                                      | T2: −395                               | T2: 1.1                                  | [10]  |
| Plasma transfer arc welding        | Nickel-based + WC                                       | 0.5 mol/L HCl                  | −448.90                                     | 365.59                                   | Ni: −346.18                            | Ni: 24.55                                | [100] |
| Plasma transfer arc welding        | Nickel-based + WC                                       | 0.5 mol/L HCl                  | −448.90                                     | 365.59                                   | Ni-30WC: −367.61                       | Ni-30WC: 9.097                           | [100] |
| Plasma transfer arc welding        | Ni60 + Ni59 + WC  | NaCl                           | N/A   | N/A                                      | 59-1: −462.58                          | 59-1: 372.3                              | [133] |
| Plasma transfer arc welding        | Ni60 + Ni59 + WC  | NaCl                           | N/A   | N/A                                      | 59-2: −375.86                          | 59-2: 318.6                              | [133] |
| Plasma transfer arc welding        | Ni60 + Ni59 + WC  | NaCl                           | N/A   | N/A                                      | 60-3: −361.1                           | 60-3: 282.5                              | [133] |
| Plasma transfer arc welding        | Ni60 + Ni59 + WC  | NaCl                           | N/A   | N/A                                      | 60-5: −317.74                          | 60-5: 259.5                              | [133] |
| LC                                 | Co-based (97wt.%Stellite-6 and 2wt.% CeO <sub>2</sub> ) | 3.5 wt.% NaCl                  | N/A   | N/A                                      | C1: −871 ± 30                          | C1: 36.48 ± 0.6                          | [36]  |
| LC                                 | Co-based (97wt.%Stellite-6 and 2wt.% CeO <sub>2</sub> ) | 3.5 wt.% NaCl                  | N/A   | N/A                                      | C2: −861 ± 20                          | C2: 29.97 ± 1.1                          | [36]  |
| LC                                 | Co-based (97wt.%Stellite-6 and 2wt.% CeO <sub>2</sub> ) | 3.5 wt.% NaCl                  | N/A   | N/A                                      | C3: −753 ± 50                          | C3: 18.93 ± 0.9                          | [36]  |

Table 8. Cont.

| Technology       | Materials  | Corrosive Medium Solution                       | Electrochemical Parameters of the Substrate |  | Electrochemical Parameters of Coatings |  | Ref.  |
|------------------|--|---|---|--|--|--|-------|
|                  |  |   | $E_{corr}$ (mV)                             | $i_{corr}$ ( $\mu\text{A}/\text{cm}^2$ ) | $E_{corr}$ (mV)                        | $i_{corr}$ ( $\mu\text{A}/\text{cm}^2$ ) |       |
| -                | -  | -   | -   | -  | -                                      | -  | -     |
| LC               | Co-based (97wt.%Stellite-6 and 2wt.% CeO <sub>2</sub> )                  | 3.5 wt.% NaCl                                   | N/A   | N/A                                      | C4: $-706 \pm 30$                      | C4: $17.40 \pm 0.7$                      | [36]  |
| LC               | Co-based (97wt.%Stellite-6 and 2wt.% CeO <sub>2</sub> )                  | 3.5 wt.% NaCl                                   | N/A   | N/A                                      | C5: $-730 \pm 40$                      | C5: $21.66 \pm 0.5$                      | [36]  |
| LC               | Ni-based   | 3.5 wt.% NaCl                                   | N/A   | N/A                                      | M: $-300.10$                           | M: $253.21$                              | [37]  |
| LC               | Ni-based   | 3.5 wt.% NaCl                                   | N/A   | N/A                                      | I: $-238.98$                           | I: $0.99$                                | [37]  |
| LC               | Ni-based   | 3.5 wt.% NaCl                                   | N/A   | N/A                                      | Z: $-376.04$                           | Z: $420.01$                              | [37]  |
| LC               | Ni-based   | 0.1% NaF  | N/A   | N/A                                      | M: $-232.60$                           | M: $295.68$                              | [37]  |
| LC               | Ni-based   | 0.1% NaF  | N/A   | N/A                                      | I: $-136.86$                           | I: $1.61$                                | [37]  |
| LC               | Ni-based   | 0.1% NaF  | N/A   | N/A                                      | Z: $-247.40$                           | Z: $782.08$                              | [37]  |
| LC               | Co-based   | 3.5 wt.% NaCl                                   | N/A   | N/A                                      | C1: $-850$                             | C1: $20.9$                               | [44]  |
| LC               | Co-based   | 3.5 wt.% NaCl                                   | N/A   | N/A                                      | C2: $-740$                             | C2: $17.1$                               | [44]  |
| LC               | Co-based   | 3.5 wt.% NaCl                                   | N/A   | N/A                                      | C3: $-670$                             | C3: $10.2$                               | [44]  |
| LC               | Co-based   | 3.5 wt.% NaCl                                   | N/A   | N/A                                      | C4: $-470$                             | C4: $5.42$                               | [44]  |
| LC               | Co-based   | 3.5 wt.% NaCl                                   | N/A   | N/A                                      | C5: $-660$                             | C5: $58.7$                               | [44]  |
| LC               | Co-based   | 3.5 wt.% NaCl                                   | N/A   | N/A                                      | C6: $-520$                             | C6: $41.5$                               | [44]  |
| LC               | Co-based   | 3.5 wt.% NaCl                                   | N/A   | N/A                                      | C7: $-530$                             | C7: $72.5$                               | [44]  |
| LC               | Co-based   | 3.5 wt.% NaCl                                   | N/A   | N/A                                      | C8: $-500$                             | C8: $44.3$                               | [44]  |
| LC               | Stellite-6   | 3.5 wt.% NaCl                                   | $-605 \pm 50$                               | $2.012 \pm 0.12 \times 10^{-3}$          | C1: $-439 \pm 30$                      | C1: $53.85 \pm 1.8$                      | [49]  |
| LC               | Stellite-6   | 3.5 wt.% NaCl                                   | $-605 \pm 50$                               | $2.012 \pm 0.12 \times 10^{-3}$          | C2: $-193 \pm 20$                      | C2: $51.52 \pm 1.1$                      | [49]  |
| LC               | Fe-based alloy powder  | 3.5 wt.% NaCl                                   | $-582$                                      | $10.80$                                  | $-494$                                 | $45.18$                                  | [57]  |
| LC               | FeCoNiCrNb <sub>0.5</sub>  | 3.5 wt.% NaCl                                   | N/A   | N/A                                      | N/A                                    | $6.212$                                  | [135] |
| LC               | FeCoNiCrNb <sub>0.5</sub> Mo <sub>0.25</sub>                             | 3.5 wt.% NaCl                                   | N/A   | N/A                                      | N/A                                    | $4.537$                                  | [135] |
| LC               | FeCoNiCrNb <sub>0.5</sub> Mo <sub>0.25</sub>                             | 3.5 wt.% NaCl                                   | N/A   | N/A                                      | N/A                                    | $3.130$                                  | [135] |
| LC               | FeCoNiCrNb <sub>0.5</sub> Mo <sub>0.25</sub>                             | 3.5 wt.% NaCl                                   | N/A   | N/A                                      | N/A                                    | $1.214$                                  | [135] |
| LC               | FeCoNiCrNb <sub>0.5</sub> Mo <sub>0.25</sub>                             | 3.5 wt.% NaCl                                   | N/A   | N/A                                      | N/A                                    | $2.144$                                  | [135] |
| Nitriding        | Aluminum nitrate   | 3.5 wt.% NaCl                                   | N/A   | N/A                                      | Plasma aluminum-nitriding: $-299.58$   | Plasma aluminum-nitriding: $0.22$        | [76]  |
| Nitriding        | Aluminum nitrate   | 3.5 wt.% NaCl                                   | N/A   | N/A                                      | Plasma nitriding: $-605.30$            | Plasma nitriding: $0.923$                | [76]  |
| Nitriding        | N <sub>2</sub> , H <sub>2</sub> , Ar                                     | A simulated seawater solution with a P.H of 8.4 | $-901$                                      | $2.38$                                   | S2: $-406$                             | S2: $0.5$                                | [136] |
| Nitriding        | N <sub>2</sub> , H <sub>2</sub> , Ar                                     | A simulated seawater solution with a P.H of 8.4 | $-901$                                      | $2.38$                                   | S3: $-369$                             | S3: $0.18$                               | [136] |
| Pack cementation | Zn, NH <sub>4</sub> Cl, Y <sub>2</sub> O <sub>3</sub> , Y-modified Zn-Fe | 3.5 wt.% NaCl                                   | N/A   | N/A                                      | Zn-Fe: $-1143.23$                      | Zn-Fe: $7.66 \times 10^{-3}$             | [132] |
| Pack cementation | Zn, NH <sub>4</sub> Cl, Y <sub>2</sub> O <sub>3</sub> , Y-modified Zn-Fe | 3.5 wt.% NaCl                                   | N/A   | N/A                                      | Y-modified Zn-Fe: $-1189.36$           | Y-modified Zn-Fe: $3.59 \times 10^{-3}$  | [132] |

## 6. Summary and Outlook

This review investigated surface modification of 42CrMo steel with a focus on enhancing wear and corrosion resistance. Surface modification techniques such as thermal spraying, deposition, hardfacing, LC, nitriding, and laser surface treatment were discussed. Materials mentioned include iron-based, cobalt-based, nickel-based, and high-entropy alloys and reinforced composite coatings. Improving coating compounds, reducing coating flaws, and creating self-lubricating coatings are all important methods for increasing the wear resistance of 42CrMo steels. The corrosion resistance of 42CrMo steels can be improved by developing corrosion-resistant coatings on the surface, rectifying coating flaws, and forming passivation films. Future research will be carried out from the following aspects.

- (1) There is a dearth of research focusing on applying HEA coatings to 42CrMo steel surfaces. By employing LC technology and adjusting the HEA material system, remarkable properties can be achieved. In this process, the process parameters of LC technology need to be studied and matched with the selected HEA materials to utilize their respective advantages. This approach has the potential to address the deficiencies inherent in 42CrMo steel.
- (2) Compared with alloy cladding, composite cladding has better wear and corrosion resistance but poorer plastic toughness. Attempts are made to improve the performance of the composite cladding by adjusting the substances and proportions contained in the composite cladding. Meanwhile, researchers are encouraged to continue to innovate surface modification methods and materials to meet the evolving challenges in wear and corrosion resistance.
- (3) Current research is mainly aimed at improving the room-temperature wear resistance of 42CrMo steel. However, for the practical application of 42CrMo steel, the improvement of high-temperature wear resistance holds greater significance. This requires consideration of the compatibility of the high-temperature-resistant material with 42CrMo steel and the ability of the technology to provide enough energy to make the material a reliable coating. Subsequent research endeavors should therefore prioritize investigations in this area.
- (4) Although some of the aforementioned materials and technologies have been applied in practical production settings, the majority remain in the experimental stage. Consequently, there is a subsequent necessity to employ diverse, complex engineering environments suitable for practical application. This involves subjecting these materials and technologies to simulations of real-world conditions, including wear-resistant and corrosion-resistant tests. Such rigorous testing is crucial for advancing the development of these materials and technologies.

**Funding:** This research was funded by the Guangdong Basic and Applied Basic Research Foundation (2023A1515011558); the Ministry of Education Chunhui Plan Project (HZKY20220434); the State Key Laboratory of Solid Lubrication Fund (LSL-2204); the Liaoning Province Natural Science Foundation (2022-YGJC-79, 2022-BS-078); and the Liaoning Province Education Department Universities Basic Scientific Research Project (LJKMZ20220345). Thanks to the Jianlong Group—Northeastern University 2023 Youth Science and Technology Innovation Fund.

**Institutional Review Board Statement:** Not applicable.

**Informed Consent Statement:** Not applicable.

**Data Availability Statement:** Data are contained within the article.

**Conflicts of Interest:** Author Guanglei Liu was employed by the company Jianlong Beiman Special Steel Co. Ltd. The remaining authors declare that the research was conducted in the absence of any commercial or financial relationships that could be construed as a potential conflict of interest.

## References

1. Wang, H.; Zhai, Y.; Zhou, L.; Zhang, Z. Study on laser surface hardening behavior of 42CrMo press brake die. *Coatings* **2021**, *11*, 997. [\[CrossRef\]](#)
2. Wu, J.; Mao, C.; Wei, K.; Hu, J. Titanium-modified plasma nitriding layer and enhanced properties for 42CrMo steel. *J. Mater. Res. Technol.* **2022**, *18*, 3819–3825. [\[CrossRef\]](#)
3. Cheng, Y.; Cui, R.; Wang, H.; Han, Z. Effect of processing parameters of laser on microstructure and properties of cladding 42CrMo steel. *Int. J. Adv. Manuf. Technol.* **2018**, *96*, 1715–1724. [\[CrossRef\]](#)
4. He, P.; Ding, Y.; Jiang, S.; Zhang, H.; Shen, T.; Wang, Y. Process parameters analysis of laser phase transformation hardening on the raceway surface of shield main bearing. *Photonics* **2023**, *10*, 287. [\[CrossRef\]](#)
5. Xiang, D.; Liu, Y.; Yu, T.; Wang, D.; Leng, X.; Wang, K.; Liu, L.; Pan, J.; Yao, S.; Chen, Z. Review on wear resistance of laser cladding high-entropy alloy coatings. *J. Mater. Res. Technol.* **2024**, *28*, 911–934. [\[CrossRef\]](#)
6. Kumar, R.K.; Kamaraj, M.; Seetharamu, S. A pragmatic approach and quantitative assessment of silt erosion characteristics of HVOF and HVOF processed WC-CoCr coatings and 16Cr5Ni steel for hydro turbine applications. *Mater. Des.* **2017**, *132*, 79–95.

7. Xu, Y.; Wang, Y.; Xu, Y.; Li, M.; Hu, Z. Microscopic characteristics and properties of Fe-based amorphous alloy compound reinforced WC-Co-based coating via plasma spray welding. *Processes* **2021**, *9*, 6. [\[CrossRef\]](#)
8. Zhang, Z.; Zhang, D.; Xie, Y. Experimental study on water droplet erosion resistance of coatings (Ni60 and WC-17Co) sprayed by APS and HVOF. *Wear* **2019**, 432–433, 202950. [\[CrossRef\]](#)
9. Sun, W.; Zhang, P.; Zhang, F.; Dong, C.; Zhang, J.; Cai, H. Influence of heat treatment on corrosion resistance of high-velocity oxygen-fuel sprayed WC-17Co coatings on 42CrMo steel. *J. Mater. Eng. Perform.* **2015**, *24*, 3218–3227. [\[CrossRef\]](#)
10. Liu, Y.; Sun, W.; Tian, S.; Xiao, Y.; Jia, Y. Microstructures and corrosion behavior of HVOF-sprayed WC-12%Cr3C2-6%Ni coatings before and after sealing. *Int. J. Appl. Ceram. Technol.* **2022**, *19*, 383–396. [\[CrossRef\]](#)
11. Liu, Y.; Sun, W.; Tian, S.; Jia, Y.; Xiao, Y. Microstructures and high-temperature friction and wear behavior of high-velocity oxygen-fuel-sprayed WC-12%Co-6%Cr coatings before and after sealing. *J. Mater. Eng. Perform.* **2022**, *31*, 448–460. [\[CrossRef\]](#)
12. Chen, Y.; Peng, X.; Kong, L.; Dong, G.; Remani, A.; Leach, R. Defect inspection technologies for additive manufacturing. *Int. J. Extrem. Manuf.* **2021**, *3*, 22002. [\[CrossRef\]](#)
13. Houdková, Š.; Smazalová, E.; Vostřák, M.; Schubert, J. Properties of NiCrBSi coating, as sprayed and remelted by different technologies. *Surf. Coat. Technol.* **2014**, *253*, 14–26. [\[CrossRef\]](#)
14. Serres, N.; Hlawka, F.; Costil, S.; Langlade, C.; Machi, F. Microstructures and mechanical properties of metallic NiCrBSi and composite NiCrBSi–WC layers manufactured via hybrid plasma/laser process. *Appl. Surf. Sci.* **2011**, *257*, 5132–5137. [\[CrossRef\]](#)
15. Chen, J.; Dong, Y.; Wan, L.; Yang, Y.; Chu, Z.; Zhang, J.; He, J.; Li, D. Effect of induction remelting on the microstructure and properties of in situ TiN-reinforced NiCrBSi composite coatings. *Surf. Coat. Technol.* **2018**, *340*, 159–166. [\[CrossRef\]](#)
16. Imanian Ghazanlou, S.; Farhood, A.H.S.; Hosouli, S.; Ahmadiyeh, S.; Rasooli, A. Pulse and direct electrodeposition of Ni–Co/micro and nanosized SiO<sub>2</sub> particles. *Mater. Manuf. Process.* **2018**, *33*, 1067–1079. [\[CrossRef\]](#)
17. Huicheng Zhang, W.Y.L.Y. Electrodeposited CoNiP coating on 42CrMo steel as gear material and its wear resistance performance in simulated oil. *Int. J. Electrochem. Sci.* **2022**, *17*, 220633. [\[CrossRef\]](#)
18. Zhang, J.; Xue, Q.; Li, S. Microstructure and corrosion behavior of TiC/Ti(CN)/TiN multilayer CVD coatings on high strength steels. *Appl. Surf. Sci.* **2013**, *280*, 626–631. [\[CrossRef\]](#)
19. Gualco, A.; Svoboda, H.G.; Surian, E.S.; Vedia, L.A.D. Effect of welding procedure on wear behaviour of a modified martensitic tool steel hardfacing deposit. *Mater. Des.* **2010**, *31*, 4165–4173. [\[CrossRef\]](#)
20. Yu, Y.X.; He, B.L.; Shi, J.P. Double metal trimming die manufactured by using hardfacing method. *Adv. Mater. Res.* **2010**, 97–101, 3940–3943. [\[CrossRef\]](#)
21. Morsy, M.A.; El-Kashif, E. Repair welding reclamation of 42CrMo4 and C45 steels. In Proceedings of the IIW 2017 International Conference, Shanghai, China, 25–30 June 2017; pp. 29–30.
22. Chen, C.; Zuo, Y.; Liu, B.; Xue, H.; Ma, B.; Li, X. Microstructure and wear resistance of nano titanium dioxide strengthening hardfacing material. *Vacuum* **2019**, *162*, 175–182. [\[CrossRef\]](#)
23. Wirth, F.; Arpagaus, S.; Wegener, K. Analysis of melt pool dynamics in laser cladding and direct metal deposition by automated high-speed camera image evaluation. *Addit. Manuf.* **2018**, *21*, 369–382. [\[CrossRef\]](#)
24. Shu, F.; Zhang, B.; Liu, T.; Sui, S.; Liu, Y.; He, P.; Liu, B.; Xu, B. Effects of laser power on microstructure and properties of laser clad CoCrBFeNiSi high-entropy alloy amorphous coatings. *Surf. Coat. Technol.* **2019**, *358*, 667–675. [\[CrossRef\]](#)
25. Zhang, H.; Pan, Y.; Zhang, Y.; Lian, G.; Cao, Q.; Yang, J. Influence of laser power on the microstructure and properties of in-situ NbC/WCoB–TiC coating by laser cladding. *Mater. Chem. Phys.* **2022**, *290*, 126636. [\[CrossRef\]](#)
26. Han, T.; Zhou, K.; Chen, Z.; Gao, Y. Research progress on laser cladding alloying and composite processing of steel materials. *Metals* **2022**, *12*, 2055. [\[CrossRef\]](#)
27. Ju, J.; Zhou, Y.; Kang, M.; Wang, J. Optimization of process parameters, microstructure, and properties of laser cladding Fe-based alloy on 42CrMo steel roller. *Materials* **2018**, *11*, 2061. [\[CrossRef\]](#)
28. Qi, K.; Yang, Y.; Sun, R.; Hu, G.; Lu, X.; Li, J. Effect of magnetic field on tribological properties of Co-based alloy layer produced by laser cladding on 42CrMo. *Mater. Lett.* **2021**, *282*, 128893. [\[CrossRef\]](#)
29. Qi, K.; Yang, Y.; Liang, W.; Jin, K.; Xiong, L. Influence of the anomalous elastic modulus on the crack sensitivity and wear properties of laser cladding under the effects of a magnetic field and Cr addition. *Surf. Coat. Technol.* **2021**, *423*, 127575. [\[CrossRef\]](#)
30. Qi, K.; Yang, Y.; Sun, R.; Hu, G.; Lu, X.; Li, J.; Liang, W.; Jin, K.; Xiong, L. Effect of magnetic field on crack control of Co-based alloy laser cladding. *Opt. Laser Technol.* **2021**, *141*, 107129. [\[CrossRef\]](#)
31. Fulin Jiang, C.L.Y.W. Effect of applied angle on the microstructure evolution and mechanical properties of laser clad 3540 Fe/CeO<sub>2</sub> coating assisted by in-situ ultrasonic vibration. *Mater. Res. Express* **2019**, *6*, 0865h6. [\[CrossRef\]](#)
32. Hu, G.; Yang, Y.; Sun, R.; Qi, K.; Lu, X.; Li, J. Microstructure and properties of laser cladding NiCrBSi coating assisted by electromagnetic-ultrasonic compound field. *Surf. Coat. Technol.* **2020**, *404*, 126469. [\[CrossRef\]](#)
33. Ur Rahman, N.; Capuano, L.; van der Meer, A.; de Rooij, M.B.; Matthews, D.T.A.; Walmag, G.; Sinnaeve, M.; Garcia-Junceda, A.; Castillo, M.; Römer, G.R.B.E. Development and characterization of multilayer laser clad high speed steels. *Addit. Manuf.* **2018**, *24*, 76–85. [\[CrossRef\]](#)
34. Ur Rahman, N.; Capuano, L.; Cabeza, S.; Feinaeugle, M.; Garcia-Junceda, A.; de Rooij, M.B.; Matthews, D.T.A.; Walmag, G.; Gibson, I.; Römer, G.R.B.E. Directed energy deposition and characterization of high-carbon high speed steels. *Addit. Manuf.* **2019**, *30*, 100838. [\[CrossRef\]](#)



35. Feng, Y.; Pang, X.; Feng, K.; Feng, Y.; Li, Z. Residual stress distribution and wear behavior in multi-pass laser clad Fe-based coating reinforced by M3(C, B). *J. Mater. Res. Technol.* **2021**, *15*, 5597–5607. [\[CrossRef\]](#)
36. Cui, C.; Wu, M.; Miao, X.; Gong, Y.; Zhao, Z. The effect of laser energy density on the geometric characteristics, microstructure and corrosion resistance of Co-based coatings by laser cladding. *J. Mater. Res. Technol.* **2021**, *15*, 2405–2418. [\[CrossRef\]](#)
37. Ray, A.; Arora, K.S.; Lester, S.; Shome, M. Laser cladding of continuous caster lateral rolls: Microstructure, wear and corrosion characterisation and on-field performance evaluation. *J. Mater. Process. Technol.* **2014**, *214*, 1566–1575. [\[CrossRef\]](#)
38. Ur Rahman, N.; de Rooij, M.B.; Matthews, D.T.A.; Walmag, G.; Sinnaeve, M.; Römer, G.R.B.E. Wear characterization of multilayer laser clad high speed steels. *Tribol. Int.* **2019**, *130*, 52–62. [\[CrossRef\]](#)
39. Qi, X.; Li, Y.; Li, F.; Du, J.; Li, C.; Wang, K.; Lu, H.; Yang, B. Improving the properties of remanufactured wear parts of shield tunneling machines by novel Fe-based composite coatings. *Ceram. Int.* **2022**, *48*, 6722–6733. [\[CrossRef\]](#)
40. Zhao, J.; Wang, G.; Wang, X.; Luo, S.; Wang, L.; Rong, Y. Multicomponent multiphase modeling of dissimilar laser cladding process with high-speed steel on medium carbon steel. *Int. J. Heat Mass Transf.* **2020**, *148*, 118990. [\[CrossRef\]](#)
41. Wan, L.; Cheng, M.; Fu, G.; Wei, C.; Shi, T.; Shi, S. Annular laser cladding of CuPb10Sn10 copper alloy for high-quality anti-friction coating on 42CrMo steel surface. *Opt. Laser Technol.* **2023**, *158*, 108878. [\[CrossRef\]](#)
42. Zhang, G.; Liu, T.; Yin, Q.; Wang, W.; Song, X.; Huang, W.; Zhang, H. Effect of B-Si ratio and laser remelting on the microstructure and properties of Fe<sub>10</sub>Co<sub>10</sub>Ni<sub>10</sub>Cr<sub>4</sub>Mo<sub>6</sub>B<sub>x</sub>Si<sub>10-x</sub> coating by laser cladding. *Surf. Coat. Technol.* **2022**, *450*, 128989. [\[CrossRef\]](#)
43. Liu, J.; Shi, Y. Microstructure and wear behavior of laser-clad Ni-based coatings decorated by graphite particles. *Surf. Coat. Technol.* **2021**, *412*, 127044. [\[CrossRef\]](#)
44. Qi, K.; Yang, Y. Microstructure, wear, and corrosion resistance of Nb-modified magnetic field-assisted Co-based laser cladding layers. *Surf. Coat. Technol.* **2022**, *434*, 128195. [\[CrossRef\]](#)
45. Qi, K.; Yang, Y.; Hu, G.; Lu, X.; Li, J. Thermal expansion control of composite coatings on 42CrMo by laser cladding. *Surf. Coat. Technol.* **2020**, *397*, 125983. [\[CrossRef\]](#)
46. Lv, G.; Yang, X.; Gao, Y.; Wang, S.; Xiao, J.; Zhang, Y.; Chen, K.; Yang, H. Investigation on fretting wear performance of laser cladding WC/Co06 coating on 42CrMo steel for hydraulic damper. *Int. J. Refract. Met. Hard Mater.* **2023**, *111*, 106068. [\[CrossRef\]](#)
47. Peng, Y.B.; Zhang, W.; Li, T.C.; Zhang, M.Y.; Wang, L.; Song, Y.; Hu, S.H.; Hu, Y. Microstructures and mechanical properties of FeCoCrNi high entropy alloy/WC reinforcing particles composite coatings prepared by laser cladding and plasma cladding. *Int. J. Refract. Met. Hard Mater.* **2019**, *84*, 105044. [\[CrossRef\]](#)
48. Wu, S.; Liu, Z.; Huang, X.; Wu, Y.; Gong, Y. Process parameter optimization and EBSD analysis of Ni60A-25% WC laser cladding. *Int. J. Refract. Met. Hard Mater.* **2021**, *101*, 105675. [\[CrossRef\]](#)
49. Cui, C.; Wu, M.; He, R.; Gong, Y.; Miao, X. Investigation on the columnar-to-equiaxed transition and corrosion behavior in multi-track Stellite-6 coating fabricated by laser cladding. *Mater. Chem. Phys.* **2022**, *291*, 126681. [\[CrossRef\]](#)
50. Feng, Y.; Yao, C.; Shen, C.; Feng, Y.; Feng, K.; Li, Z. Influence of in-situ synthesized carboborides on microstructure evolution and the wear resistance of laser clad Fe-base composite coatings. *Mater. Charact.* **2020**, *164*, 110326. [\[CrossRef\]](#)
51. Zhang, N.; Xu, Y.; Wang, M.; Hou, X.; Du, B.; Ge, X.; Shi, H.; Xie, X. M2 coating prepared by ultra-high speed laser cladding: Microstructure and interfacial residual stress. *Mater. Today Commun.* **2023**, *35*, 105638. [\[CrossRef\]](#)
52. Kaiming, W.; Yulong, L.; Hanguang, F.; Yongping, L.; Zhenqing, S.; Pengfei, M. A study of laser cladding NiCrBSi/Mo composite coatings. *Surf. Eng.* **2018**, *34*, 267–275. [\[CrossRef\]](#)
53. Yingtao, Z.; Yongliang, M.; Gang, W.; Xiulin, J.; Zhichao, L. Experimental study on the wear properties of 42CrMo steel with different microstructures and T15 laser cladding. *J. Mater. Eng. Perform.* **2022**, *31*, 4232–4241. [\[CrossRef\]](#)
54. Kai-ming, W.; Han-guang, F.; Yu-long, L.; Yong-ping, L.; Shi-zhong, W.; Zhen-qing, S. Effect of power on microstructure and properties of laser cladding NiCrBSi composite coating. *Trans. IMF* **2017**, *95*, 328–336. [\[CrossRef\]](#)
55. Hu, G.; Yang, Y.; Qi, K.; Lu, X.; Li, J. Investigation of the microstructure and properties of NiCrBSi coating obtained by laser cladding with different process parameters. *Trans. Indian Inst. Met.* **2020**, *73*, 2623–2634. [\[CrossRef\]](#)
56. Wang, K.; Chang, B.; Lei, Y.; Fu, H.; Lin, Y. Effect of cobalt on microstructure and wear resistance of Ni-based alloy coating fabricated by laser cladding. *Metals* **2017**, *7*, 551. [\[CrossRef\]](#)
57. Xu, H.; Lu, H.; Zhang, H.; Xiao, G.; Zhao, W. Laser cladding in-situ nano-submicron TiC reinforced ultrafine-grained Fe-based composite layers on 42CrMo steel. *Int. J. Electrochem. Sci.* **2019**, *14*, 9974–9981. [\[CrossRef\]](#)
58. Shu, D.; Cui, X.; Li, Z.; Sun, J.; Wang, J.; Chen, X.; Dai, S.; Si, W. Effect of the rare earth oxide CeO<sub>2</sub> on the microstructure and properties of the nano-WC-reinforced Ni-based composite coating. *Metals* **2020**, *10*, 383. [\[CrossRef\]](#)
59. Wang, H.; Zhang, W.; Peng, Y.; Zhang, M.; Liu, S.; Liu, Y. Microstructures and wear resistance of FeCoCrNi-Mo high entropy alloy/diamond composite coatings by high speed laser cladding. *Coatings* **2020**, *10*, 300. [\[CrossRef\]](#)
60. Wang, D.; Chu, J.; Qu, G.; Zhou, X. Preparation and characterization of laser clad NiCrBSi coating reinforced with WC. *J. Phys. Conf. Ser.* **2021**, *1965*, 12110. [\[CrossRef\]](#)
61. Yinghua, L.; Kaiming, W. Microstructure and properties of a laser clad NiCrBSi alloy coating. *Numer. Simul.* **2021**, *62*, 698–702. [\[CrossRef\]](#)
62. Xu, L.; Xiao, R.; Qu, G.; Wang, D. In situ synthesized graded TiC particulate reinforced Ni-based composite coating prepared by laser cladding. *J. Phys. Conf. Ser.* **2021**, *1820*, 12050. [\[CrossRef\]](#)
63. Zhang, Y.; Ma, Y.; Duan, M.; Wang, G.; Li, Z. The improvement of the wear resistance of T15 laser clad coating by the uniformity of microstructure. *Lubricants* **2022**, *10*, 271. [\[CrossRef\]](#)

64. Liu, Z.; Yin, F.; Chen, C.; Zhao, L.; Fu, L.; Feng, Y.; Cao, Y.; Peng, Y.; Tian, Z.; Li, C. Microstructure and wear resistance of a Cr7C3 reinforced Ni3Al composite coating prepared by laser cladding. *Coatings* **2022**, *12*, 105. [\[CrossRef\]](#)
65. Cai, Z.; Zhang, P.; Liang, X.; Tantai, F.; Yang, F. Research of microstructure and performance of laser cladding Fe-based medium manganese alloy. In Proceedings of the 2015 4th International Conference on Mechatronics, Materials, Chemistry and Computer Engineering, Xi'an, China, 12–13 December 2015; Atlantis Press: Amsterdam, The Netherlands, 2015; pp. 944–949.
66. Rahman, N.U.; Capuano, L.; Rooij, M.B.D.; Matthews, D.T.A.; Garcia-Junceda, A.; Mekicha, M.A.; Cordova, L.; Walmag, G.; Sinnaeve, M.; Römer, G.R.B.E. Laser metal deposition of vanadium-rich high speed steel: Microstructural and high temperature wear characterization. *Surf. Coat. Technol.* **2019**, *364*, 115–126. [\[CrossRef\]](#)
67. Li, Y.; Liu, Z.; Luo, J.; Zhang, S.; Qiu, J.; He, Y. Microstructure, mechanical and adhesive properties of CrN/CrTiAlSiN/WCrTiAlN multilayer coatings deposited on nitrided AISI 4140 steel. *Mater. Charact.* **2019**, *147*, 353–364. [\[CrossRef\]](#)
68. Wu, J.; Liu, H.; Li, J.; Yang, X.; Hu, J. Comparative study of plasma oxynitriding and plasma nitriding for AISI 4140 steel. *J. Alloys Compd.* **2016**, *680*, 642–645. [\[CrossRef\]](#)
69. Li, Y.; Wang, L.; Shen, L.; Zhang, D.; Wang, C. Plasma nitriding of 42CrMo low alloy steels at anodic or cathodic potentials. *Surf. Coat. Technol.* **2010**, *204*, 2337–2342. [\[CrossRef\]](#)
70. Wang, B.; Zhao, X.; Li, W.; Qin, M.; Gu, J. Effect of nitrided-layer microstructure control on wear behavior of AISI H13 hot work die steel. *Appl. Surf. Sci.* **2018**, *431*, 39–43. [\[CrossRef\]](#)
71. Mao, C.; Wei, K.; Liu, X.; Yu, X.; Hu, J. A novel titanium enhanced plasma nitriding for 42CrMo steel. *Mater. Lett.* **2020**, *262*, 127052. [\[CrossRef\]](#)
72. Tang, L.; Mao, C.; Jia, W.; Wei, K.; Hu, J. The effect of novel composite pretreatment on performances of plasma nitrided layer. *J. Mater. Res. Technol.* **2020**, *9*, 9531–9536. [\[CrossRef\]](#)
73. Tang, L.; Jia, W.; Hu, J. An enhanced rapid plasma nitriding by laser shock peening. *Mater. Lett.* **2018**, *231*, 91–93. [\[CrossRef\]](#)
74. Kovacı, H.; Hacısalihoğlu, İ.; Yetim, A.F.; Çelik, A. Effects of shot peening pre-treatment and plasma nitriding parameters on the structural, mechanical and tribological properties of AISI 4140 low-alloy steel. *Surf. Coat. Technol.* **2019**, *358*, 256–265. [\[CrossRef\]](#)
75. Kang, Q.; Fan, H.; Yang, X.; An, X.; Hu, J. Evolution of aluminum hydroxide film during plasma nitriding and its enhancement effect. *Mater. Lett.* **2023**, *330*, 133348. [\[CrossRef\]](#)
76. Kang, Q.; Wei, K.; Fan, H.; Liu, X.; Hu, J. Ultra-high efficient novel plasma aluminum-nitriding methodology and performances analysis. *Scr. Mater.* **2022**, *220*, 114902. [\[CrossRef\]](#)
77. Liu, H.; Li, J.; Sun, F.; Hu, J. Characterization and effect of pre-oxidation on D.C. plasma nitriding for AISI4140 steel. *Vacuum* **2014**, *109*, 170–174. [\[CrossRef\]](#)
78. Li, J.; Yang, X.; Wang, S.; Wei, K.; Hu, J. A rapid D.C. plasma nitriding technology catalyzed by pre-oxidation for AISI4140 steel. *Mater. Lett.* **2014**, *116*, 199–202. [\[CrossRef\]](#)
79. Mirjani, M.; Mazrooei, J.; Karimzadeh, N.; Ashrafizadeh, F. Investigation of the effects of time and temperature of oxidation on corrosion behavior of plasma nitrided AISI 4140 steel. *Surf. Coat. Technol.* **2012**, *206*, 4389–4393. [\[CrossRef\]](#)
80. Ebrahimi, M.; Sohi, M.H.; Raouf, A.H.; Mahboubi, F. Effect of plasma nitriding temperature on the corrosion behavior of AISI 4140 steel before and after oxidation. *Surf. Coat. Technol.* **2010**, *205*, S261–S266. [\[CrossRef\]](#)
81. Heydarzadeh Sohi, M.; Ebrahimi, M.; Honarbakhsh Raouf, A.; Mahboubi, F. Comparative study of the corrosion behaviour of plasma nitrocarburised AISI4140 steel before and after post-oxidation. *Mater. Des.* **2010**, *31*, 4432–4437. [\[CrossRef\]](#)
82. Sun, P.; Li, S.; Yu, G.; He, X.; Zheng, C.; Ning, W. Laser surface hardening of 42CrMo cast steel for obtaining a wide and uniform hardened layer by shaped beams. *Int. J. Adv. Manuf. Technol.* **2014**, *70*, 787–796. [\[CrossRef\]](#)
83. Li, C.; Wang, Y.; Han, B. Microstructure, hardness and stress in melted zone of 42CrMo steel by wide-band laser surface melting. *Opt. Lasers Eng.* **2011**, *49*, 530–535. [\[CrossRef\]](#)
84. Chaowen, L.; Yong, W.; Bin, H.; Tao, H.; Huanxiao, Z. Numerical simulation of multi-track laser surface melting of 42CrMo steel. In Proceedings of the 2010 International Conference on Computer Design and Applications, Qinhuaingdao, China, 25–27 June 2010; pp. 65–69.
85. Weng, F.; Chen, C.; Yu, H. Research status of laser cladding on titanium and its alloys: A review. *Mater. Des.* **2014**, *58*, 412–425. [\[CrossRef\]](#)
86. Wang, Y.; Zhao, S.; Gao, W.; Zhou, C.; Liu, F.; Lin, X. Microstructure and properties of laser cladding FeCrBSi composite powder coatings with higher Cr content. *J. Mater. Process. Technol.* **2014**, *214*, 899–905. [\[CrossRef\]](#)
87. Lu, J.Z.; Cao, J.; Lu, H.F.; Zhang, L.Y.; Luo, K.Y. Wear properties and microstructural analyses of Fe-based coatings with various WC contents on H13 die steel by laser cladding. *Surf. Coat. Technol.* **2019**, *369*, 228–237. [\[CrossRef\]](#)
88. Lizzul, L.; Sorgato, M.; Bertolini, R.; Ghiotti, A.; Bruschi, S.; Fabbro, F.; Rech, S. On the influence of laser cladding parameters and number of deposited layers on as-built and machined AISI H13 tool steel multilayered claddings. *CIRP J. Manuf. Sci. Technol.* **2021**, *35*, 361–370. [\[CrossRef\]](#)
89. Shang, X.; Liu, Q.; Guo, Y.; Ding, K.; Liao, T.; Wang, F. Nano-TiC reinforced [Cr-Fe<sub>4</sub>Co<sub>4</sub>Ni<sub>4</sub>]Cr<sub>3</sub> high-entropy-alloy composite coating fabricated by laser cladding. *J. Mater. Res. Technol.* **2022**, *21*, 2076–2088. [\[CrossRef\]](#)
90. Zhu, L.; Xu, B.; Wang, H.; Wang, C. Microstructure and nanoindentation measurement of residual stress in Fe-based coating by laser cladding. *J. Mater. Sci.* **2012**, *47*, 2122–2126. [\[CrossRef\]](#)
91. Zhao, J.; Gao, Q.; Wang, H.; Shu, F.; Zhao, H.; He, W.; Yu, Z. Microstructure and mechanical properties of Co-based alloy coatings fabricated by laser cladding and plasma arc spray welding. *J. Alloys Compd.* **2019**, *785*, 846–854. [\[CrossRef\]](#)

92. Chen, J.; Guo, M.; Yang, M.; Su, H.; Liu, L.; Zhang, J. Phase-field simulation of  $\gamma'$  coarsening behavior in cobalt-based superalloy. *Comput. Mater. Sci.* **2021**, *191*, 110358. [\[CrossRef\]](#)
93. Han, J.; Yoo, B.; Im, H.J.; Oh, C.; Choi, P. Microstructural evolution of the heat affected zone of a Co–Ti–W alloy upon laser cladding with a CoNiCrAlY coating. *Mater. Charact.* **2019**, *158*, 109998. [\[CrossRef\]](#)
94. Qin, R.; Zhang, X.; Guo, S.; Sun, B.; Tang, S.; Li, W. Laser cladding of high Co–Ni secondary hardening steel on 18Cr2Ni4WA steel. *Surf. Coat. Technol.* **2016**, *285*, 242–248. [\[CrossRef\]](#)
95. Cui, G.; Han, B.; Zhao, J.; Li, M. Comparative study on tribological properties of the sulfurizing layers on Fe, Ni and Co based laser cladding coatings. *Tribol. Int.* **2019**, *134*, 36–49. [\[CrossRef\]](#)
96. Yu, H.; Ukai, S.; Hayashi, S.; Oono, N.H. Effect of Cr and Y<sub>2</sub>O<sub>3</sub> on the oxidation behavior of Co-based oxide dispersion strengthened superalloys at 900 °C. *Corros. Sci.* **2017**, *127*, 147–156. [\[CrossRef\]](#)
97. Lin, Y.; Liu, Y. Effects of Co and W on the microstructure and wear behavior of NiCrAlMoTiFeNbX equimolar multicomponent-clad layers. *Wear* **2020**, *446–447*, 203186. [\[CrossRef\]](#)
98. Yue, H.; Lv, N.; Guo, C.; Zhai, J.; Dai, W.; Zhang, J.; Zhao, G. Multi-objective process optimization of laser cladding Co-based alloy by process window and grey relational analysis. *Coatings* **2023**, *13*, 1090. [\[CrossRef\]](#)
99. Lyu, Y.; Sun, Y.; Yang, Y. Non-vacuum sintering process of WC/W<sub>2</sub>C reinforced Ni-based coating on steel. *Met. Mater. Int.* **2016**, *22*, 311–318. [\[CrossRef\]](#)
100. Liu, S.; Chen, H.; Zhao, X.; Fan, L.; Guo, X.; Yin, Y. Corrosion behavior of Ni-based coating containing spherical tungsten carbides in hydrochloric acid solution. *J. Iron Steel Res. Int.* **2019**, *26*, 191–199. [\[CrossRef\]](#)
101. Li, X.; Zhu, W.; Shen, H.; Cai, J.; Guan, Q.; Lyu, P.; Li, Y. Microstructures and high-temperature oxidation behavior of laser clad NiCoCrAlYSi coating on Inconel 625 Ni-based superalloy modified via high current pulsed Electron beam. *Surf. Coat. Technol.* **2021**, *427*, 127796. [\[CrossRef\]](#)
102. Liu, K.; Li, Y.; Wang, J. In-situ reactive fabrication and effect of phosphorus on microstructure evolution of Ni/Ni–Al intermetallic composite coating by laser cladding. *Mater. Des.* **2016**, *105*, 171–178. [\[CrossRef\]](#)
103. Chang, F.; Cai, B.; Zhang, C.; Huang, B.; Li, S.; Dai, P. Thermal stability and oxidation resistance of FeCr<sub>x</sub>CoNiB high-entropy alloys coatings by laser cladding. *Surf. Coat. Technol.* **2019**, *359*, 132–140. [\[CrossRef\]](#)
104. Cai, Y.; Zhu, L.; Cui, Y.; Geng, K.; Manladan, S.M.; Luo, Z.; Han, J. Strengthening mechanisms in multi-phase FeCoCrNiAl<sub>1.0</sub> high-entropy alloy cladding layer. *Mater. Charact.* **2020**, *159*, 110037. [\[CrossRef\]](#)
105. Lu, K.; Zhu, J.; Guo, D.; Yang, M.; Sun, H.; Wang, Z.; Hui, X.; Wu, Y. Microstructures, corrosion resistance and wear resistance of high-entropy alloys coatings with various compositions prepared by laser cladding: A review. *Coatings* **2022**, *12*, 1023.
106. Kuang, S.; Zhou, F.; Liu, W.; Liu, Q. Al<sub>2</sub>O<sub>3</sub>/MC particles reinforced MoFeCrTiWNbx high-entropy-alloy coatings prepared by laser cladding. *Surf. Eng.* **2022**, *38*, 158–165. [\[CrossRef\]](#)
107. Yuan, S.; Li, H.; Han, C.; Li, W.; Xu, X.; Chen, C.; Wei, R.; Wang, T.; Wu, S.; Li, F. FeCoNiCrAl<sub>0.6</sub> high-entropy alloy coating on Q235 steel fabricated by laser cladding. *Mater. Sci. Technol.* **2023**, *39*, 705–713. [\[CrossRef\]](#)
108. Peng, Y.; Zhang, W.; Li, T.; Zhang, M.; Wang, L.; Hu, S. Microstructures and wear-resistance of WC-reinforced high entropy alloy composite coatings by plasma cladding: Effect of WC morphology. *Surf. Eng.* **2021**, *37*, 678–687. [\[CrossRef\]](#)
109. Peng, Y.; Zhang, W.; Li, T.; Zhang, M.; Liu, B.; Liu, Y.; Wang, L.; Hu, S. Effect of WC content on microstructures and mechanical properties of FeCoCrNi high-entropy alloy/WC composite coatings by plasma cladding. *Surf. Coat. Technol.* **2020**, *385*, 125326. [\[CrossRef\]](#)
110. Tan, D.Q.; Yang, X.Q.; He, Q.; Mo, J.L.; Zhuang, W.H.; He, J.F. Impact-sliding wear properties of PVD CrN and WC/C coatings. *Surf. Eng.* **2021**, *37*, 12–23. [\[CrossRef\]](#)
111. Tillmann, W.; Hagen, L.; Kokalj, D. Embedment of eutectic tungsten carbides in arc sprayed steel coatings. *Surf. Coat. Technol.* **2017**, *331*, 153–162. [\[CrossRef\]](#)
112. Zhang, T.G.; Zhuang, H.F.; Zhang, Q.; Yao, B.; Yang, F. Influence of Y<sub>2</sub>O<sub>3</sub> on the microstructure and tribological properties of Ti-based wear-resistant laser-clad layers on TC4 alloy. *Ceram. Int.* **2020**, *46*, 13711–13723. [\[CrossRef\]](#)
113. Sun, S.; Fu, H.; Ping, X.; Guo, X.; Lin, J.; Lei, Y.; Wu, W.; Zhou, J. Effect of CeO<sub>2</sub> addition on microstructure and mechanical properties of in-situ (Ti, Nb)C/Ni coating. *Surf. Coat. Technol.* **2019**, *359*, 300–313. [\[CrossRef\]](#)
114. Liu, Y.; Yang, L.; Yang, X.; Zhang, T.; Sun, R. Optimization of microstructure and properties of composite coatings by laser cladding on titanium alloy. *Ceram. Int.* **2021**, *47*, 2230–2243. [\[CrossRef\]](#)
115. Cui, C.; Wu, M.; He, R.; Gong, Y.; Miao, X. Effect of CeO<sub>2</sub> addition on grain refinement and mechanical properties of stellite-6 coating fabricated by laser cladding. *J. Therm. Spray Technol.* **2022**, *31*, 2621–2634. [\[CrossRef\]](#)
116. Yan, L.; Guan, L.; Wang, D.; Xiang, D. Application and prospect of wear simulation based on ABAQUS: A review. *Lubricants* **2024**, *12*, 57. [\[CrossRef\]](#)
117. Wang, K.; Liu, W.; Li, X.; Tong, Y.; Hu, Y.; Hu, H.; Chang, B.; Ju, J. Effect of hot isostatic pressing on microstructure and properties of high chromium K648 superalloy manufacturing by extreme high-speed laser metal deposition. *J. Mater. Res. Technol.* **2024**, *28*, 3951–3959. [\[CrossRef\]](#)
118. Yang, K.; Bao, Y. Improving high-temperature wear resistance of Fe–Cr<sub>13</sub>–C hardfacing alloy by nitrogen alloying. *Steel Res. Int.* **2013**, *84*, 457–462. [\[CrossRef\]](#)
119. Xiang, D.; Wang, D.; Zheng, T.; Chen, Y. Effects of rare earths on microstructure and wear resistance in metal additive manufacturing: A review. *Coatings* **2024**, *14*, 139. [\[CrossRef\]](#)

120. Yin, C.; Liang, Y.; Liang, Y.; Li, W.; Yang, M. Formation of a self-lubricating layer by oxidation and solid-state amorphization of nano-lamellar microstructures during dry sliding wear tests. *Acta Mater.* **2019**, *166*, 208–220. [[CrossRef](#)]
121. Sivalingam, V.; Zan, Z.; Sun, J.; Selvam, B.; Gupta, M.K.; Jamil, M.; Mia, M. Wear behaviour of whisker-reinforced ceramic tools in the turning of Inconel 718 assisted by an atomized spray of solid lubricants. *Tribol. Int.* **2020**, *148*, 106235. [[CrossRef](#)]
122. Akhtar, S.S. A critical review on self-lubricating ceramic-composite cutting tools. *Ceram. Int.* **2021**, *47*, 20745–20767. [[CrossRef](#)]
123. Zhu, S.; Cheng, J.; Qiao, Z.; Yang, J. High temperature solid-lubricating materials: A review. *Tribol. Int.* **2019**, *133*, 206–223. [[CrossRef](#)]
124. Dou, P.; Jia, Y.; Zheng, P.; Wu, T.; Yu, M.; Reddyhoff, T.; Peng, Z. Review of ultrasonic-based technology for oil film thickness measurement in lubrication. *Tribol. Int.* **2022**, *165*, 107290. [[CrossRef](#)]
125. Huang, Q.; Shi, X.; Xue, Y.; Zhang, K.; Gao, Y.; Wu, C. Synergetic effects of biomimetic microtexture with multi-solid lubricants to improve tribological properties of AISI 4140 steel. *Tribol. Int.* **2022**, *167*, 107395. [[CrossRef](#)]
126. Liu, X.; Guo, Z.; Lu, Z.; Qin, L. Tribological behavior of the wear-resistant and self-lubrication integrated interface structure with ordered micro-pits. *Surf. Coat. Technol.* **2023**, *454*, 129159. [[CrossRef](#)]
127. Sun, J.; Wang, D.; Yang, J.; Li, F.; Zuo, L.; Ge, F.; Chen, Y. In situ preparation of nano-Cu/microalloyed gradient coating with improved antifriction properties. *Coatings* **2022**, *12*, 1336. [[CrossRef](#)]
128. Ma, H.; Wei, K.; Zhao, X.; Liu, X.; Hu, J. Performance enhancement by novel plasma boron-nitriding for 42CrMo4 steel. *Mater. Lett.* **2021**, *304*, 130709. [[CrossRef](#)]
129. Zheng, X.; Zheng, K.; Chang, J.; Qu, S.; Jia, W.; Li, Z.; Yu, S.; Gao, J.; Ma, Y. Microstructure, mechanical properties and reciprocating wear properties of diamond grits-reinforced NiCrBSi composite coatings on 42CrMo. *Surf. Coat. Technol.* **2022**, *445*, 128703. [[CrossRef](#)]
130. Suge, M.; Baolin, Z.; Zhefeng, Z.; Xiangwen, C.; Cuiyong, T. Effect of excitation coil voltage on TiAlSiN coating on 42CrMo steel surface. *Mater. Res. Express* **2020**, *7*, 56519. [[CrossRef](#)]
131. Liu, Y.; Xiang, D.; Wang, K.; Yu, T. Corrosion of laser cladding high-entropy alloy coatings: A review. *Coatings* **2022**, *12*, 1669. [[CrossRef](#)]
132. Liu, L.; Yu, S.; Cao, W. Zn-Fe and Y-modified Zn-Fe coatings on 42CrMo steel via pack cementation. *Rare Met.* **2021**, *40*, 2266–2274. [[CrossRef](#)]
133. Fan, L.; Chen, H.Y.; Du, H.L.; Hou, Y.; Cheng, Q. Corrosion resistance of nickel-based composite coatings reinforced by spherical tungsten carbide. *Mater. Sci. Forum* **2020**, *993*, 1075–1085. [[CrossRef](#)]
134. Wan, T.; Huang, Z.; Cheng, Z.; Zhu, M.; Zhu, W.; Li, Z.; Fu, D.; Fuzeng, R. The effect of chromium content on the corrosion behavior of ultrafine-grained CrxMnFeCoNi high-entropy alloys in sulfuric acid solution. *Microstructures* **2023**, *3*, 2023014.
135. Zhou, Z.; Jiang, F.; Yang, F.; Yang, Y.; Liang, P. Novel laser cladding FeCoNiCrNb<sub>0.5</sub>Mo<sub>x</sub> high-entropy alloy coatings with excellent corrosion resistance. *Mater. Lett.* **2023**, *335*, 133714. [[CrossRef](#)]
136. Valdés, J.; Huape, E.; Oseguera, J.; Ruíz, A.; Ibarra, J.; Bernal, J.L.; Medina, A. Effects of plasma nitriding in the corrosion behavior of an AISI 4140 steel using a seawater medium solution. *Mater. Lett.* **2022**, *316*, 131991. [[CrossRef](#)]

**Disclaimer/Publisher’s Note:** The statements, opinions and data contained in all publications are solely those of the individual author(s) and contributor(s) and not of MDPI and/or the editor(s). MDPI and/or the editor(s) disclaim responsibility for any injury to people or property resulting from any ideas, methods, instructions or products referred to in the content.